Weyl formula: Experimental test of ray splitting and corner corrections

C. Vaa,[1] P. M. Koch,[1] and R. Blümel[2]
[1]*Department of Physics and Astronomy, Stony Brook University, Stony Brook, New York 11794-3800, USA*
[2]*Department of Physics, Wesleyan University, Middletown, Connecticut 06459-0155, USA*
(Received 9 June 2005; published 17 November 2005)

The number of resonances $N(f)$ of a resonator below frequency f is an essential concept in physics. Smooth approximations $\bar{N}(f)$ are known as Weyl formulas. An abrupt change in the properties of the wave propagation medium in a resonator was predicted by Prange *et al.* [Phys. Rev. E **53**, 207 (1996)] to produce a universal ray-splitting correction to $\bar{N}(f)$. We confirm this effect experimentally. Our results with a quasi-two-dimensional dielectric-loaded microwave cavity are directly relevant to the ray-splitting correction in two-dimensional quantal ray-splitting billiards. Our experimental spectra have sufficient accuracy and extent to allow, as far as we are aware, the first experimental determination of the corner correction, which we find to agree with theory. We show that our movable-bar setup enhances non-Newtonian periodic orbits, thereby providing an experimental technique for periodic-orbit spectroscopy. This technique, differential spectroscopy, will facilitate the study of non-Newtonian classical physics.

DOI: 10.1103/PhysRevE.72.056211 PACS number(s): 05.45.−a, 03.65.Sq

I. INTRODUCTION

Physics and mathematics give and take. Seventeenth century mathematics, e.g., profited enormously from advances in physics and astronomy that led to the development of calculus by Newton and Leibnitz [1]. Today string theory drives important developments in mathematics [2]. The direction reverses in the case of differential geometry and Yang-Mills theories. Einstein's general theory of relativity [3] profited from advances in 19th century differential geometry; Yang-Mills theory, which is the point of departure for modern particle physics [4], came on the scene three decades after Weyl's introduction of the idea of a gauge field [5].

The subject of this paper, Weyl formulas, is a fine example of physics driving mathematics. Kac's well known paper [6] includes the tale of its beginnings, upon which we build next [7]. (More history into the 1970s is in [8].) Dates will alert the reader to the rapidity of early events. The rise of quantum physics early in the 20th century made the computation of the number of electromagnetic modes in a perfectly conducting cavity a hot topic for theorists. At the end of the fourth in his series of six Wolfskehl Lectures to a mixed audience of physicists and mathematicians in Göttingen during 24–29 October 1910, Lorentz conjectured that in the high-frequency limit, and to leading order in the frequency f, the number of modes between f and $f+df$ in an electromagnetic cavity is determined by its volume V, independent of its *shape* [9]. To support his conjecture Lorentz mentions explicit calculations carried out for a Leiden dissertation for some analytically calculable resonators (parallelepiped, sphere, and cylinder) though the paper does not mention the name of the researcher. According to mathematics lore (Kac mentions "an apocryphal report" in Ref. [6], p. 4) the Göttingen host Hilbert predicted after the lecture that the proof of Lorentz's conjecture would not be done in his lifetime. Weyl, whose 1908 mathematics Ph.D. had been supervised by Hilbert, met the challenge within four months. Applying Hilbert's theory of integral equations, Weyl reported in a communication received on 20 February 1911 [10] his proof for the two-dimensional (2D) version of Lorentz's conjecture.

The final section of Weyl's subsequent detailed paper [11] includes his proof for the case of the 3D electromagnetic cavity conjectured by Lorentz. However, as is now well known [8, p. 16], Weyl's proof in [11,12] addresses an "ersatz cavity" having incorrect boundary conditions for the electromagnetic problem. The asymptotic formula that Weyl obtained for the number of (ersatz) modes below f (in Hz),

$$\bar{N}(f) = \frac{8\pi V}{3c^3} f^3, \tag{1}$$

with c the speed of light in the resonator, is fortuitously the same as the correct formula obtained for the 3D electromagnetic problem with the correct boundary conditions [13].

Surprisingly, only recently was Weyl's result [11] submitted to an experimental test. The first experimental check of the 3D electromagnetic formula, including the surface-curvature correction term discovered by Balian and Bloch [13], appeared in 1995 [14], more than eight decades after Weyl had established his result [11]. Using irregularly shaped cavities, the authors of Ref. [14] checked Weyl's asymptotic (volume) formula, both its frequency dependence and its insensitivity to the shape of the resonator, the main point of Weyl's proof [11] of Lorentz's conjecture [9].

Weyl's first footnote in [11] cites as prior influential work a 1905 paper by Jeans [15], a lecture delivered by Lorentz at the 1908 International Mathematics Congress in Rome [16], the aforementioned lectures of Lorentz in Göttingen [9], and results in acoustics presented by Arnold Sommerfeld in 1910 [17]. It also names the student, "Fräulein Reudler," who did the calculations supporting Lorentz's conjecture [9]. Her dissertation defended in Leiden on 21 May 1912 [18] completes a circle and cites Weyl's first paper [10].

More papers from Weyl appeared soon after [12,19–21]. Courant and Hilbert included Weyl's work in their celebrated

mathematical physics textbook [22] in 1924, thus establishing its general importance already one year before the discovery of quantum mechanics. Bound-state spectra of the Schrödinger equation then joined the growing list of applications for Weyl formulas.

Following Weyl's proof, mode-counting formulas continued as an important subject in acoustics, where obtaining an accurate measure for the number of levels in an "air-filled room" (with damping) as a function of frequency has practical importance, e.g., for a theoretical explanation [23–26] of the empirical Sabine law [27] for reverberation [[28], Sec. VIII.33]. Because concert halls are often constructed in irregular shapes [27] that make computing their resonance frequencies difficult, a formula that determines $\bar{N}(f)$ is useful. However, because of the relatively slow speed of sound (c_s=344 m/s [29] for air at standard atmospheric pressure, 20 °C temperature, 40% relative humidity, and typical CO_2 concentration), for audio frequencies, roughly 20 Hz–20 kHz, even a room-sized chamber is not in the asymptotic regime where just the volume term in the Weyl formula is sufficient. [For compression waves the acoustical field has only one polarization state, so its asymptotic 3D Weyl formula is one-half of Eq. (1).]

The first derivations of the correction to the volume term of the Weyl formula for an undamped 3D chamber were published in back-to-back papers in the Journal of the American Acoustical Society in 1939 by Bolt [30] (see also [31]) and Maa [32], working independently. Each published a different formula for counting the number of acoustic eigenmodes as a function of frequency for a rectangular parallelepiped chamber with dimensions L_x, L_y, and L_z. Bolt's formula is

$$\bar{N}(f)^{\mathrm{3D}}_{\mathrm{Bolt}} = \frac{4\pi V}{3c_s^3} f^3 \left(\frac{2fV + c_s R^{1/2}}{2fV + \frac{1}{2} c_s R^{1/2}} \right)^3, \tag{2}$$

where $R=(L_xL_y)^2+(L_yL_z)^2+(L_zL_x)^2$.

Maa's formula is

$$\bar{N}(f)^{\mathrm{3D}}_{\mathrm{Maa}} = \frac{4\pi V}{3c_s^3} f^3 + \frac{\pi S}{4c_s^2} f^2 + \frac{L_x + L_y + L_z}{2c_s} f - \frac{7}{8}, \tag{3}$$

where S is the surface area of the resonator. Maa introduces the constant term in Eq. (3) to avoid counting the zero-frequency mode, which "is not vibratory at all" [32]. To our knowledge this makes Maa the first to include, in modern parlance, a *corner correction*; see Sec. VIII.

Bolt and Maa cited each other's work and knew that their different formulas give similar results to graphical accuracy, as Bolt showed in Fig. 7 of [30]. As historical notes we remark that (i) Roe [26] confirmed Maa's formula (but Roe left out the constant term) and extended the treatment to some other calculable shapes; (ii) the first edition of Morse's textbook [28], which influenced both Bolt and Maa, does not go beyond the "volume term" for the rectangular room, though later editions [33,34] of the book and Sec. 15 in the 1944 review article of Morse and Bolt [35] did reproduce Eq. (3) save for the constant term.

Though Refs. [23,24,35] did, the papers cited in the previous paragraph did not explicitly cite Weyl's work but, instead, cited Courant and Hilbert [22], which cites and discusses Weyl's work. Consisting of a sum of terms that can be clearly identified as originating from the volume, the surface and some characteristic linear dimensions of the resonator, Maa's formula has the "modern" form for a Weyl formula for a 3D system with Neumann boundary conditions [8,36].

Applying Bolt's result (2) to a cubic resonator ($L_x=L_y=L_z$) and making a Taylor series expansion in powers of f reveals that the term $\sim f^2$ differs from the surface term in Maa's formula (3) by a factor $\sqrt{3}/2$. Since Maa's formula (3), which is based on a simple lattice-point-counting technique [22], is correct to all orders of f that appear in Eq. (3), we conclude that Bolt's formula is wrong in the sense that apart from the volume term it makes incorrect predictions for the surface, length, and corner corrections of a 3D acoustic resonator.

To our knowledge Bolt made the first experimental measurement to demonstrate the need for the leading (length) correction term for a 2D acoustic chamber [37]. He derived a formula for the number of modes for such a quasi two-dimensional (Q2D) resonator,

$$\bar{N}(f)^{\mathrm{2D}}_{\mathrm{Bolt}} = \frac{\pi A}{c_s^2} f^2 \left(\frac{2fA + c_s L}{2fA + (c_s/2)L} \right)^2, \tag{4}$$

where $A=L_xL_y$ is the cross-sectional area, and $L \equiv (L_x^2+L_y^2)^{1/2}$ is the length of the hypotenuse of a right triangle with sides of length L_x and L_y, respectively. He compared this to his measurements of $N(f)$, finding much improvement over a formula, $\bar{N}(f)=\pi A f^2/c_s^2$, that takes into account only the area A of the resonator. Work done on 3D resonators three decades later by Balian and Bloch [13] showed that the constant multiplying the length term depends on whether the boundary of the resonator is smooth or has sharp edges.

Since the times of Weyl, Bolt, and Maa many researchers studied Weyl formulas, i.e., the average behavior of the number of modes in various acoustic, electrodynamic, and quantum resonators [8]. Weyl's original asymptotic formula takes only the volume of the resonator into account. But even the first correction term to the Weyl formula, proportional to the surface area of the resonator [see e.g., Eq. (3)] is not sufficiently accurate for some physical applications. Consequently many additional correction terms to the Weyl formula were derived [8]. These correction terms depend on fine geometrical details of the resonator such as the curvature of its surface and its genus.

In 1996 Prange *et al.* [38] postulated a new correction term to the Weyl formula: the *ray-splitting correction*; see also [39,40]. This correction was predicted to be important for all resonators with discontinuities in the properties of the resonator's wave propagation medium. The purpose of this paper is to give a full report of the results of our experiments which prove the existence of the ray-splitting (RS) correction in the case of a dielectric-loaded Q2D microwave cavity [41–43]. In addition we present material on the experimental extraction of the corner correction (Sec. VIII) and the statistics of our resonance spectra (Sec. IX).

The plan of this paper is as follows. In Sec. II we briefly review the theory of ray splitting in as much detail as neces-

sary for a self-contained presentation of our experimental and theoretical results. In Sec. II A we review the equivalence between quantum billiards and Q2D microwave resonators, first shown by Stöckmann and Stein [44]. This provides the opportunity for us to introduce notation and to set the stage for the development of material presented in later sections. In Sec. II B we present the Weyl formula for a quantum step billiard. For the convenience of the reader and reference in later sections, we translate all quantum formulas into "microwave language," expressing them in terms of microwave frequencies and dielectric constants. In Sec. III we motivate our experiments. The detailed implementation of our experiment is presented in Sec. IV. Apart from the details of the design of our cavity (Secs. IV A–IV C) we present details on the properties and fabrication of the dielectric inserts of our cavity (Sec. IV D), the measurements of their dielectric constants (Sec. IV E), and the generation and detection of the microwave fields (Sec. IV F). In Sec. V we discuss the importance of the completeness of our microwave resonance spectra. We argue that even a single missing or additional (spurious) resonance would make the determination of the RS correction impossible. In Sec. VI we present our results on the extraction of the ray-splitting correction to the Weyl formula from experimentally measured resonance spectra of our Q2D dielectric-loaded microwave cavity. In Sec. VII we study the localization of wave functions in our cavity and find types of localized states that we conjecture are typical for dielectric-loaded microwave cavities but do not occur in empty cavities. As far as its Q2D physics is concerned, our Q2D microwave cavity has, effectively, four metallic corners which, according to the theoretical results presented in Sec. II, should result in a corner correction to the Weyl formula, a constant of magnitude 1/4. In Sec. VIII we present the extraction of the corner correction to the Weyl formula; to our knowledge this is the first time the corner correction is extracted from an experimental resonance spectrum. In Sec. IX we examine the nearest-neighbor spacing statistics of our measured resonances and find consistency with Poissonian statistics. In Sec. X we investigate the manifestation of Newtonian and non-Newtonian periodic orbits in the Fourier transform of our resonance spectra. On the basis of these results we are able to explain the origin of both fine oscillations and coarse undulations in the measured RS data presented in Sec. VI. In Sec. XI we discuss our results. In Sec. XII we present some interesting research directions which show that the study of Weyl formulas in RS systems is far from exhausted. In Sec. XIII we summarize our results and conclude the paper.

II. THEORY

Ray splitting is a wave-mechanical phenomenon that occurs whenever a wave encounters a discontinuity in the propagation medium and splits into two or more rays (usually) traveling away from the discontinuity [45]. Lateral rays [46,47] are an exception; they travel along the discontinuity. Ray splitting can occur in many types of systems. It can occur in a microwave cavity (or any optical system) with a discontinuity in electric permittivity, a discontinuity in magnetic permeability, or both. An electromagnetic wave impinging on an air/dielectric boundary, e.g., will, in general, be partially transmitted and partially reflected. In acoustic systems, a wave in an elastic medium can split into a shear wave and a pressure wave when it hits a boundary inside of the medium [45]. This is an example where an incoming ray is split into more than two outgoing rays.

In the context of classical mechanics we expect that in a system with ray splitting particle orbits are possible which would not be possible without ray splitting. We refer to these orbits as *non-Newtonian* orbits [48] since they are orbits which are not contained in Newton's classical mechanics. Ray splitting has been shown to produce non-Newtonian orbits both theoretically [45] and experimentally [48].

Consider, for example, a quantum particle with energy $E > V_0$ incident from the left ($x < 0$) on a potential step $V = V_0\theta(x)$, where

$$\theta(x) = \begin{cases} 0 & \text{for } x < 0, \\ \frac{1}{2} & \text{for } x = 0, \\ 1 & \text{for } x > 0. \end{cases} \tag{5}$$

The particle has probability amplitude

$$r = \frac{\sqrt{E} - \sqrt{E - V_0}}{\sqrt{E} + \sqrt{E - V_0}} \tag{6}$$

for being reflected off the step and back to the $V=0$ side of the potential (above-barrier reflection). We are interested in the short-wavelength limit ($\lambda \to 0$) in the limit of a sharp step ($a \to 0$). The result of this double limit ($a \to 0$, $\lambda \to 0$) depends on the order in which we take the limits. If we first let $\lambda \to 0$ and *then* let $a \to 0$, the proper classical mechanics in the short-wavelength limit is Newton's classical mechanics. This, however, is not the correct ordering of limits to obtain an RS problem. Ray-splitting problems demand that we *first* let $a \to 0$ and *then* let $\lambda \to 0$. In this case, since (6) is independent of λ (independent of $\hbar$), the reflection coefficient r is nonzero even for $\lambda = 0$. This implies that there is *above-barrier classical reflection* from the potential step, a feature not contained in Newton's mechanics. Clearly a non-Newtonian, nondeterministic classical mechanics is required for a proper description of the physics of RS systems in the classical limit. In particular, the nondeterministic mechanics properly describes *classical* reflection off the potential step, and thus predicts the existence of non-Newtonian classical (periodic) orbits, which were subsequently identified experimentally in the resonance spectrum of a dielectric-loaded Bunimovich cavity [48,49]. More details on the ordering of limits and the non-Newtonian classical mechanics can be found in Ref. [50].

A. Equivalence between quantum billiards and Q2D microwave cavities

In this section we study the physics of dielectric-loaded, flat Q2D microwave cavities and relate them to two-dimensional quantum billiards with energy-scaling potentials. The cavities we focus on are rectangular, right parallelepipeds with length L, width W, and height H, where H is

much smaller than both L and W. Both empty and dielectric-loaded Q2D cavities were already used by many researchers [43,44,48,49,51–59] to study resonance spectra as analog systems of quantum chaotic billiard problems [36,60]. As described in [44] the vector Helmholtz equation for the electromagnetic field in a Q2D electromagnetic resonator of arbitrary cross-sectional shape [61] reduces to a scalar Helmholtz equation for the z component E_z of the electric field (parallel to the height). In Ref. [38] it was shown that the equivalence holds even in cases where the resonator contains dielectric inserts.

For cavities completely filled with a material having dielectric constant $\kappa_e=\epsilon/\epsilon_0$ and relative magnetic permeability $\kappa_m=\mu/\mu_0$, where ϵ (μ) is the permittivity (permeability) of the material and ϵ_0 (μ_0) is the permittivity (permeability) of vacuum ($c^2\mu_0\epsilon_0=1$), the equivalence holds for frequencies below the 3D cutoff frequency

$$f_{3\mathrm{D}}^{\min} > f_{3\mathrm{D}}^{\infty} = \frac{c}{2H\sqrt{\kappa_e\kappa_m}}, \tag{7}$$

where $f_{3\mathrm{D}}^{\infty}$ is the limiting case for $L,W\to\infty$ with finite H. Using as an example the air-filled ($\kappa_e^{\mathrm{air}}-1=5.7\times10^{-4}$ [62]; $\kappa_m^{\mathrm{air}}-1=3.1\times10^{-8}$ [63]) cavity with dimensions $L,W,H=H_2=4.341$ cm given in Sec. IV A, $f_{3\mathrm{D}}^{\min}=3.4603$ GHz, slightly above $f_{3\mathrm{D}}^{\infty}=3.4520$ GHz. For resonators partially filled with dielectric, $f_{3\mathrm{D}}^{\min}$ is more difficult to estimate, but Eq. (7) provides a safe lower limit.

Let us define, respectively, κ_e^a,κ_e^w to be the relative permittivities of air and wax; λ_0, λ_a, and λ_w to be the wavelengths in vacuum, air, and wax; k_0, k_a, and k_w to be the wave numbers in vacuum, air, and wax; and c, c_a, and c_w to be the speeds of light in vacuum, air, and wax. We assume a flat cavity throughout this section and approximate $\kappa_e^a=\kappa_m^a=1$. Assuming negligible loss, the refractive indices $n_{a,w}=\sqrt{\kappa_e^{a,w}}$ are real, and with f denoting the microwave frequency we have $c_{a,w}=c/n_{a,w}$, $\lambda_{a,w}=c_{a,w}/f$, $k_{a,w}=2\pi/\lambda_{a,w}=k_0\sqrt{\kappa_e^{a,w}}$.

In air- (wax-)filled regions we must solve

$$(\Delta_2+k_{a,w}^2)E_z(x,y)=(\Delta_2+k_0^2\kappa_e^{a,w})E_z(x,y)=0, \tag{8}$$

respectively, where $\Delta_2=\partial^2/\partial x^2+\partial^2/\partial y^2$ is the two-dimensional Laplacian operator. Defining

$$\kappa_e(x,y)=\begin{cases}\kappa_e^a & \text{for air-filled regions,}\\ \kappa_e^w & \text{for wax-filled regions,}\end{cases} \tag{9}$$

which describes the distribution of dielectric in the cavity, we combine the two equations (8) into

$$[\Delta_2+k_0^2\kappa_e(x,y)]E_z(x,y)=0. \tag{10}$$

Defining $\psi(x,y)\equiv E_z(x,y)$ and

$$V(E;x,y)=E[1-\kappa_e(x,y)], \tag{11}$$

the Helmholtz equation (10) can be written in the form of an energy-scaling Schrödinger equation

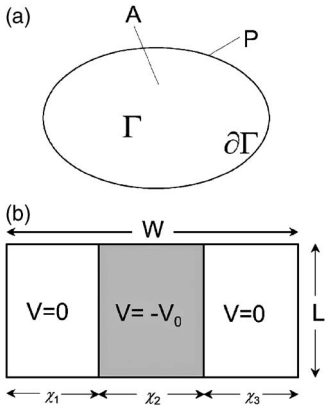

FIG. 1. Examples of quantum billiards. (a) General quantum billiard Γ with perimeter $\partial\Gamma$. The area of the billiard is A, the length of its perimeter is P. (b) Quantum-well billiard of width W and length L. The width of the well is χ_2 and its depth is $V=-V_0$. The widths of the zero-potential areas of the quantum-well billiard are χ_1 and χ_3, respectively.

$$-\frac{\hbar^2}{2m}\Delta_2\psi(x,y)+V(E_{\mathrm{mech}};x,y)\psi(x,y)=E_{\mathrm{mech}}\psi(x,y), \tag{12}$$

where $E_{\mathrm{mech}}=\hbar^2k_0^2/2m$ is the mechanical energy of a quantum particle in vacuum.

The potential (11) has linear energy dependence. We call such potentials *energy scaling* potentials. They are of great importance in the study of quantum chaos because for them the classical phase space is invariant under changes of the energy E. This avoids the problem of phase-space metamorphoses [64] and thus guarantees that even for changing E quantum wave functions are always associated with the same, invariant classical phase-space structures. As is argued in Ref. [65], this is of particular importance for producing nearest-neighbor spacing statistics [36,60] of the quantum spectrum, where one analyzes the statistics of sequences of energy levels for varying energy, but would ideally like to make a one-to-one correspondence of the nearest-neighbor spacing statistics with a given, unchanging morphology of the underlying classical phase space [65]. Using scaled energy level statistics solves this problem.

B. Ray-splitting correction to the Weyl formula

A two-dimensional quantum billiard [see Fig. 1(a)] is a compact (finite) region Γ of the two-dimensional plane with a quantum particle confined within. The wave function of this quantum particle satisfies the scalar Helmholtz-Schrödinger equation

$$\Delta_2\psi(x,y)+k^2\psi(x,y)=0, \tag{13}$$

where k is the wave number and $E=k^2$ is the energy. Specifying boundary conditions on ψ turns (13) into a spectral problem. We consider two types of boundary conditions for ψ on the boundary $\partial\Gamma$ of Γ: (i) $\psi(x,y)|_{\partial\Gamma}=0$ (Dirichlet) and $\partial\psi(x,y)/\partial\vec{n}|_{\partial\Gamma}=0$, where $\vec{n}$ is the normal on $\partial\Gamma$ (Neumann).

It can be shown [66] that (13) subject to Dirichlet (Neumann) boundary conditions has a countably infinite spectrum

of solutions $\psi_n(x,y)$, $n=1,2,\ldots$, with associated energies E_n, $n=1,2,\ldots$. The spectral staircase is defined as

$$N(E)=\sum_{n=1}^{\infty}\theta(E-E_n), \tag{14}$$

where θ is the θ function (5). Weyl showed [10,11] that to leading order the staircase function $N(E)$ can be approximated by a smooth function $\bar{N}(E)=AE/(4\pi)$, where A is the area of the quantum billiard. As discussed in the Introduction, additional terms were derived later, such that "Weyl's formula" now reads

$$\bar{N}(E)=\frac{AE}{4\pi}\mp\frac{P\sqrt{E}}{4\pi}+\bar{N}_{\mathrm{corr}}(E), \tag{15}$$

where P is the perimeter of the billiard (the length of $\partial\Gamma$), and $\bar{N}_{\mathrm{corr}}(E)$ includes correction terms that depend on the geometrical details of the billiard, such as its topology, the curvature of its boundary, or the number and opening angles of its corners [8].

We now switch on a potential in the interior of the billiard. In particular we consider the case of a rectangular billiard of length L and width W [see Fig. 1(b)] with

$$V(x,y)=\begin{cases}0 & \text{for } 0<x<\chi_1 \quad \text{or} \quad \chi_1+\chi_2<x<W,\\ -V_0 & \text{for } \chi_1<x<\chi_1+\chi_2.\end{cases} \tag{16}$$

For the case $V_0<0$ the staircase function $\bar{N}(E)$ is derived in [67]. In the context of the present paper we need $\bar{N}(E)$ for $V_0>0$. It consists of

$$\bar{N}(E)=\bar{N}_A(E)+\bar{N}_P(E)+\bar{N}_{\mathrm{RS}}(E)+\bar{N}_{\mathrm{RSJ}}(E)+\bar{N}_C(E), \tag{17}$$

where the five terms on the right-hand side (RHS) of (17) are, respectively, the area term, the perimeter term, the RS term, the correction due to RS junctions [67], and the net corner correction term due to four metallic corners, respectively. For $V_0>0$ they are given explicitly by

$$\bar{N}_A(E)=\frac{A_0E}{4\pi}\theta(E)+\frac{A_V(E+V_0)}{4\pi}\theta(E+V_0), \tag{18}$$

$$\bar{N}_P(E)=\mp\frac{P_0\sqrt{E}}{4\pi}\theta(E)\mp\frac{P_V\sqrt{E+V_0}}{4\pi}\theta(E+V_0), \tag{19}$$

$$\bar{N}_{\mathrm{RS}}(E)=L\sqrt{V_0}\Bigg\{-\frac{1}{4\pi}\Bigg[\theta(E+V_0)\sqrt{\frac{E+V_0}{V_0}}+\theta(E)\sqrt{\frac{E}{V_0}}\Bigg]+\frac{1}{\pi^2}\theta(E)\sqrt{\frac{E+V_0}{V_0}}\mathcal{E}\Bigg(\sqrt{\frac{V_0}{E+V_0}}\Bigg)+\frac{1}{\pi^2}\theta(-E)\times\Bigg[\mathcal{E}\Bigg(\sqrt{\frac{E+V_0}{V_0}}\Bigg)+\Bigg(\frac{E}{V_0}\Bigg)\mathcal{K}\Bigg(\sqrt{\frac{E+V_0}{V_0}}\Bigg)\Bigg]\Bigg\}, \tag{20}$$

$$\bar{N}_{\mathrm{RSJ}}(E)=\pm\Bigg[\frac{1}{4}[\theta(E+V_0)-\theta(E)]-\frac{1}{\pi}\arcsin\Bigg(\sqrt{\frac{E+V_0}{V_0}}\Bigg)\theta(-E)\Bigg], \tag{21}$$

$$\bar{N}_C(E)=\frac{1}{4}, \tag{22}$$

where $A_0=L(\chi_1+\chi_3)$, $A_V=L\chi_2$, $P_0=2(\chi_1+\chi_3+L)$, $P_V=2\chi_2L$, and $\mathcal{K},\mathcal{E}$ are, respectively, the complete elliptic integrals of the first and second kind [68].

The corrections (20) and (21) are theoretical predictions that, so far, have not yet been checked experimentally for quantum systems. However, a RS correction to the Weyl formula exists in all wave problems in which the propagation medium has sudden spatial changes. In particular we expect a RS correction to be present in electromagnetic resonators that are partially filled with dielectrics having edges that are sharp on the scale of the wavelength. We showed above that the Maxwell equations for a Q2D dielectric-loaded electromagnetic resonator is formally identical with the Schrödinger equation of a two-dimensional quantum billiard in the presence of the energy-scaling potential (11). This analogy allows us to derive the staircase function for a Q2D microwave cavity with a rectangular dielectric bar insert [see Fig. 2(a)]. Substituting $V_0=(\kappa_e-1)E$ into the quantum results (18)–(21), converting energy to frequency according to $E=k_0^2=4\pi^2f^2/c^2$, approximating $\kappa_e^{\mathrm{air}}=1$ for simplicity (see Sec. II A for a justification), and using $E>0$ and $E+V_0=\kappa_eE>0$, we arrive at

$$\bar{N}(f)=\bar{N}_A(f)+\bar{N}_P(f)+\bar{N}_{\mathrm{RS}}(f)+\bar{N}_{\mathrm{RSJ}}(f)+\bar{N}_C(f), \tag{23}$$

where

$$\bar{N}_A(f)=\frac{\pi}{c^2}(A_0+\kappa_eA_{\mathrm{bar}})f^2, \tag{24}$$

$$\bar{N}_P(f)=\mp\frac{1}{2c}(P_0+\sqrt{\kappa_e}P_{\mathrm{bar}})f, \tag{25}$$

$$\bar{N}_{\mathrm{RS}}(f)=\frac{L}{2c}\nu(\kappa_e)f, \tag{26}$$

$$\nu(\kappa_e)=\frac{4\sqrt{\kappa_e}}{\pi}\mathcal{E}\Bigg(\sqrt{\frac{\kappa_e-1}{\kappa_e}}\Bigg)-1-\sqrt{\kappa_e}, \tag{27}$$

$$\bar{N}_{\mathrm{RSJ}}(f)=0, \tag{28}$$

$$\bar{N}_C(f)=\frac{1}{4}. \tag{29}$$

Here $A_0=L(a+e-d)$, $A_{\mathrm{bar}}=L(d-a)$, $P_0=2(L+a+e-d)$, and $P_{\mathrm{bar}}=2(d-a)$. The function $\nu(\kappa_e)$ determines the size of the RS correction. Figure 3 shows it for $1\leqslant\kappa_e\leqslant5$. We note that because of $E>0$ and $E+V_0>0$ the first two θ functions in (21) cancel, and the third θ function is zero, resulting in

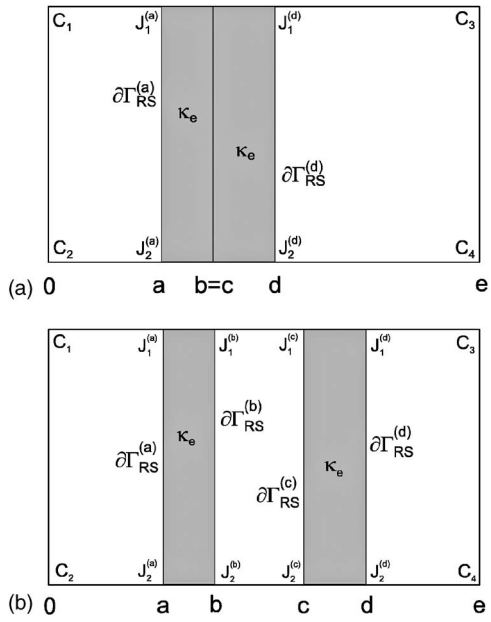

FIG. 2. Schematic sketch of our movable-bar experiment consisting of two dielectric bars simultaneously present in the cavity. (a) "Bars-together" configuration; (b) "bars-apart" configuration. Both configurations (a) and (b) have four metallic corners denoted by $C_1,\ldots,C_4$, respectively. The four RS boundaries in the bars-apart configuration (b) are denoted by $\partial\Gamma_{RS}^{(a)}$, $\partial\Gamma_{RS}^{(b)}$, $\partial\Gamma_{RS}^{(c)}$, $\partial\Gamma_{RS}^{(d)}$, respectively, the eight RS junctions by $J_{1,2}^{(a)},\ldots,J_{1,2}^{(d)}$, respectively. In the bars-together configuration (a) only two RS boundaries ($\partial\Gamma_{RS}^{(a)}$ and $\partial\Gamma_{RS}^{(d)}$) are present. The different number of RS boundaries in the bars-apart and bars-together configurations is the key to our experiment.

$\bar{N}_{RSJ}=0$. As discussed in the following section this fact will turn out to be of great importance for our experiments.

III. PLANNING THE EXPERIMENT: DESIGN CRITERIA

A. General remarks

To plan the Q2D cavity experiment we considered the factors most strongly affecting the final design. Foremost is the realization that the RS correction to the Weyl formula is a small effect even compared to the perimeter term. For the dielectric-loaded Q2D rectangular cavity shown in Fig. 2(a), e.g., we obtain

$$\left|\frac{\bar{N}_{RS}}{\bar{N}_P}\right| < \frac{1}{2}\nu(\kappa_e). \tag{30}$$

For the value $\kappa_e^w=2.236(13)$ used in our experiments (see Sec. IV E), Fig. 3 shows that the expected RS correction is less than 2% of the perimeter correction. The estimate (30), together with (25) and (26), shows that although $\bar{N}_{RS}$ is proportional to L, building a larger cavity is not necessarily a good idea because the ratio of $\bar{N}_{RS}$ and $\bar{N}_P$ depends only on the aspect ratios of the cavity and is independent of its size. The following argument, however, shows that in our case a larger cavity is better. From Eq. (26) we see that even for a

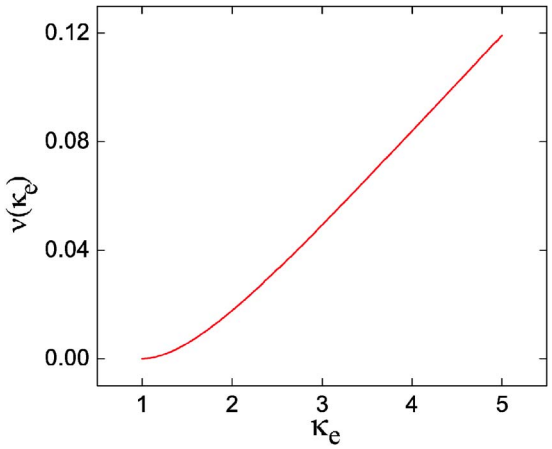

FIG. 3. (Color online) The dimensionless function $\nu(\kappa_e)$ defined in Eq. (27) for $1<\kappa_e<5$.

"large" cavity, one with linear dimensions on the order of a meter, and for a microwave frequency up to a few gigahertz, $\bar{N}_{RS}$ is well below 1. But it is well known [8,14] that the staircase function $N(f)$ fluctuates around its average $\bar{N}(f)$. These fluctuations far exceed the signal, $\bar{N}_{RS}(f)$, we wish to detect. To increase the signal-to-fluctuations ratio and extract $\bar{N}_{RS}(f)$, we must average $N(f)$ over many resonances. Once the amplitude of fluctuations is reduced by averaging, we profit by making $\bar{N}_{RS}$ as large as possible. Since according to Eq. (26), $\bar{N}_{RS}$ is directly proportional to L, this argues for a large cavity.

Thus, a key design criterion for our experiment is a cavity that is quasi-2D over as large a frequency range as possible. This calls for a cavity with one dimension small and two dimensions large, on the order of a meter. The experimental spectral resolution must also be high enough to resolve near degeneracies. The competing requirements of quasi-2D-ness and high-resolution necessitate a compromise.

One expression for the quality factor of a resonance is

$$Q=\frac{f}{\Delta f}, \tag{31}$$

where Δf is the full width at half maximum of the Lorentzian line shape centered at frequency f. High resolution means small Δf which means large Q.

A scaling relation [69] for the (unloaded) quality factor Q_0 is

$$Q_0 \sim \frac{V}{S\delta}, \tag{32}$$

where V is the volume of the cavity interior where field energy is stored and $S\delta$ is the volume in the cavity walls where energy is dissipated, with S the surface area and

$$\delta=\sqrt{\frac{2\epsilon_0 c^2}{\sigma\omega}} \tag{33}$$

the skin (or penetration) depth, $\epsilon_0=8.85\times10^{-12}$ C^2/N m^2 being the permittivity of free space, c the speed of light, σ the

conductivity of the metal walls, and $\omega=2\pi/f$. High conductivity metal is desirable for cavity construction because it has a small skin depth and the fields do not penetrate far into the cavity walls. This lowers losses. The calculated skin depth at room temperature and 1 GHz, a typical frequency in our experiments, is $\delta=2.1$ μm for copper and $\delta=2.7$ μm for aluminum.

The expectation of a small experimental signal strongly influences the shape of the cavity. To facilitate computational support we choose a rectangular parallelepiped with relatively large length L and width W and small height H. Decreasing H raises f_{3D}^{∞}, which is good, but it decreases V/S, which decreases Q_0, increases Δf, and spoils the resolution, which is bad. Section IV A gives the actual dimensions used to realize the compromise.

B. How to extract the RS correction experimentally

1. A single-bar experiment will not work

At this point a possible experimental setup would consist of a large but thin rectangular Q2D cavity with a rectangular dielectric bar insert as shown in Fig. 2(a). This single-bar setup recalls earlier experiments with a dielectric-loaded Q2D cavity [48,49]. Extraction of the RS correction from it would use the following three steps: (i) Measure the experimental staircase function $N(f)$; (ii) subtract $\bar{N}_A(f)+\bar{N}_P(f)+\bar{N}_{\mathrm{RSJ}}+\bar{N}_C$ from $N(f)$, leaving the fluctuating quantity $N_{\mathrm{RS}}(f)$ containing the RS correction; (iii) smooth $N_{\mathrm{RS}}(f)$ sufficiently to reveal its average behavior, i.e., $\bar{N}_{\mathrm{RS}}(f)$. Though it works well for the computational extraction of the RS correction of various quantum RS billiards [67,70], we find that the three-step method does not work for the experimental determination of the RS correction.

It works for the model systems discussed in [67,70] because the area and perimeter terms of the Weyl formula are known with zero error. To work experimentally, however, the measurements of the linear dimensions of the cavity, and the cavity alignments, would have to be known and controlled with supreme precision in order not to overwhelm the RS correction (a very small effect) with the contributions from imprecisely known area and perimeter terms. One might propose that instead of measuring the cavity geometry mechanically, e.g., with calipers, a more accurate determination of the area and perimeter terms would be achieved by fitting the expressions (24) and (25) to the measured staircase function $N(f)$ and then, by subtracting the fitted $\bar{N}_A(f)$ and $\bar{N}_P(f)$ from $N(f)$, extract accurate values for the cavity geometry directly from the smoothed difference. Indeed, given a sufficient number of measured resonances an accurate value for the area term could be obtained because $\bar{N}_A(f)$ is proportional to f^2 whereas all the other contributions to $\bar{N}(f)$ are proportional to lower powers of f. This would allow the contribution of the area term to be separated from all other contributions to $\bar{N}(f)$. Unfortunately it is not possible to separate the perimeter term $\bar{N}_P(f)$ from the RS correction since according to Eqs. (25) and (26) both have the same (linear) dependence on the frequency. Therefore, the fitting does not work either.

2. A two-movable-bar experiment will work

Realizing that with our resources a straightforward implementation of the theoretical three-step procedure for extracting the RS correction will fail, we perform a *movable bar* experiment. Instead of working with a single dielectric-bar insert as shown in Fig. 2(a), we load the cavity with two dielectric bars as shown in Fig. 2(b). With the two bars set apart as shown in Fig. 2(b), there are four RS boundaries, denoted by $\partial\Gamma_{\mathrm{RS}}^{(a)},\ldots,\partial\Gamma_{\mathrm{RS}}^{(d)}$. Pushing the bars together as shown in Fig. 2(a) eliminates two RS boundaries, $\partial\Gamma_{\mathrm{RS}}^{(b)}$ and $\partial\Gamma_{\mathrm{RS}}^{(c)}$. Thus, the difference between the two staircase functions,

$$\Delta N(f)=N_{\mathrm{apart}}(f)-N_{\mathrm{together}}(f), \tag{34}$$

contains twice the contribution of a single RS boundary without the necessity of knowing any of the cavity's dimensions. This key idea is the enabling technology of our experiment. The movable-bar technique will work because it is easier to keep the cavity dimensions constant than to determine their absolute values.

However, pulling the bars apart not only generates two new RS boundaries $\partial\Gamma_{\mathrm{RS}}^{(b)}$ and $\partial\Gamma_{\mathrm{RS}}^{(c)}$, but also generates four new RS junctions, labeled $J_{1,2}^{(b)}$ and $J_{1,2}^{(c)}$ in Fig. 2(b). Fortunately, according to Eq. (28), the theoretical contribution of each RS junction of the dielectric bar inserts to $\bar{N}(f)$ is zero, so their total number is immaterial. Subject to experimental confirmation (see Sec. VIII), $\Delta N(f)$ contains only the contribution from the two additional RS boundaries.

Though the movable-bar technique eliminates the need for precise knowledge of the actual cavity dimensions, it does not eliminate the strong fluctuations in the individual staircase functions $N_{\mathrm{apart}}(f)$ and $N_{\mathrm{together}}(f)$ that lead to large fluctuations (on the order of three states) in the difference staircase (34). However, integrating $\Delta N(f)$ over frequency introduces sufficient smoothing in $\Delta N(f)$ to allow reliable extraction of the RS correction $\bar{N}_{\mathrm{RS}}(f)$ to the Weyl formula.

In summary, our experimental protocol involves measuring the integrated difference

$$I^{(\mathrm{expt})}(f)=\int_0^f \Delta N(f')df'. \tag{35}$$

The average of $\Delta N(f)$ contains the average contribution of two RS boundaries. Therefore, with Eq. (26), an analytical prediction for $\bar{I}^{(\mathrm{expt})}(f)$ is given by

$$\bar{I}^{(\mathrm{ana})}(f)=2\int_0^f \bar{N}_{\mathrm{RS}}(f')df'=\frac{L}{2c}\nu(\kappa_e)f^2. \tag{36}$$

A null result for $\bar{I}^{(\mathrm{expt})}(f)$ would indicate absence of a RS correction to the Weyl formula, whereas a significant, nonzero $\bar{I}^{(\mathrm{expt})}(f)$ of approximately quadratic behavior in f would experimentally prove its existence. Though we are still sensitive to fluctuations that survive the integration smoothing, the method does not require us to fit the staircase function.

FIG. 4. (Color online) Photograph of our experimental setup. The four aluminum bars put on the top lid to help prevent lid buckling (see Sec. VI D) were removed for the photograph. Note the thin aluminum strips. They direct the downward force of the steel clamps to make good electrical contact between the copper-coated circuit board and the inside edge of each side-wall bar.

Thus, no assumptions concerning the analytical structure of $\bar{N}(f)$ are required: our movable-bar method amounts to a model-independent procedure for extracting the RS correction.

IV. IMPLEMENTATION OF THE EXPERIMENT

This section provides details of the experimental setup that we built following the design criteria developed in the preceding section.

A. Cavity geometry

Figure 4 shows a photograph of the cavity used to measure the RS correction to the Weyl formula. Two large sheets of electronic circuit board form the top and bottom, and four aluminum bars form the sides. Two paraffin wax bars within the cavity create the dielectric discontinuities that cause RS. Homemade steel clamps hold the pieces together with good electrical contact and make the cavity lie flat on a steel optical table.

We chose the rectangular parallelepiped shape for the cavity because this facilitates calculation of its spectrum, both empty and with rectangular dielectric inserts present, and it simplifies construction. As motivated in Sec. III, the cavity length L and width W were chosen as large as possible given the constraints imposed by available sizes for sheets of circuit board and the size of the optical table. Final measured dimensions are $L=96.048(8)$ cm and $W=82.69(4)$ cm. We chose the cavity height H as a compromise between the quality factor Q and the 3D onset frequency $f_{3D}^{\min}$; see Eq. (7) and Sec. II A. We chose $H_2=4.341\pm0.003$ cm, which gives measured Q values of a few thousand and $f_{3D}^{\min}>2.3$ GHz.

B. Top and bottom lids

Since it is of uniform thickness and is easily obtained in large $(1\times1\ \mathrm{m}^2)$ sheets, we chose to use electronic circuit board for the top and bottom lids of the cavity. Type FR4 board (old name "G-10") is 1/16″ thick fiberglass and epoxy-resin laminated on one side with a 2 oz/ft^2 copper coating, which corresponds to a thickness of 2.8 mils (71 μm). The skin depth of copper at the lowest resonance frequency of the cavity (about 200 MHz) is $\delta=4.7$ μm, which is much smaller than the thickness of the copper coating.

C. Cavity walls

Because it has low losses (small skin depth) over our experimental frequency range and is inexpensive, readily available, and easily machined, we chose aluminum for the four cavity side walls. To provide spare bars for other uses in the experiment (see Sec. IV E), we ordered eight bars, each about 1.75 in. wide, cut from 1.5 in. 6061-T6 aluminum alloy plate. Through the sides of each rough-cut bar we drilled four to six antenna holes at random positions; the chosen hole diameter, 3.6 mm, provides a snug fit for semirigid (copper) coaxial cable antennas that we used to couple microwave power in and out of the cavity. In the end faces of each rough-cut bar we drilled and tapped matching holes that allow the bars to be firmly bolted together to form the cavity.

Four plane surfaces (with rectangular cross section $H_1\times H_2$) were ground on each of the eight bars. Corresponding dimensions for all eight bars had to be within 0.002 in. of each other, and the transverse dimensions had to lie within a 0.020 in. window around 1.490 in. (H_1) and 1.710 in. (H_2), respectively. We specified that the final surface finish be 32 microin. or better and that the corners be left "sharp" (no deburring).

The finished, transverse dimensions are $H_1\times H_2=3.772(3)\times4.341(3)$ cm^2. We specified the two values of H to provide two choices for the Q versus $f_{3D}^{\min}$ "height compromise" (see Sec. III A), but it turned out that we used H_2 for taking all data.

D. Wax bars

Previous experiments in our laboratory [48,51] used Teflon ($\kappa_e^{\mathrm{Teflon}}=2.07$) to produce RS. Though Teflon is an excellent choice for relatively small dielectric inserts, it is not a good choice for the present experiment, which needs large dielectric bars [71]. Instead, we chose paraffin wax as the dielectric inserts since it is cheap, readily available, has small losses, and can be molded easily into desired shapes. To make the mold into which molten wax is poured, we clamped the four "spare" ground aluminum bars (see preceding section) onto a large, flat piece of aluminum honeycomb-cored panel (used to make floors in aircraft) donated by Lunn Industries.

Our application requires that the wax bars be uniform in height. We solved this problem by molding each wax bar with a height everywhere exceeding the cavity height (H_2) followed by "machining" the top surface of the wax bar with a plastic straightedge used as a scraper. Because the straightedge "rode" on the aluminum bars used to make the mold, we could make the final height of each wax bar satisfactorily close to H_2.

TABLE I. Measurements of the average (and standard deviation) $\bar{\kappa}_e^w$ (column 6) for wax bars B_1 and B_2 (identified in column 1) in mode numbers (n,m). Given mode number m (column 2) N_{id} resonances (column 4) were identified lying in an n range specified in column 3, which corresponds to the κ_e^w range listed in column 5.

Bar	m	n range	N_{id}	κ_e^w range	$\bar{\kappa}_e^w$ (σ)
B_1	1	$1 \leqslant n \leqslant 21$	18	2.2454–2.2494	2.2483(11)
	2	$2 \leqslant n \leqslant 19$	18	2.2405–2.2475	2.2447(16)
	3	$1 \leqslant n \leqslant 15$	15	2.2406–2.2481	2.2438(17)
	4	$2 \leqslant n \leqslant 5$	3	2.2406–2.2429	2.2418(11)
B_2	1	$1 \leqslant n \leqslant 21$	19	2.2237–2.2403	2.2355(46)
	2	$2 \leqslant n \leqslant 19$	17	2.2247–2.2372	2.2308(24)
	3	$1 \leqslant n \leqslant 15$	14	2.2351–2.2456	2.2388(24)
	4	$1 \leqslant n \leqslant 8$	7	2.2375–2.2490	2.2424(43)

We also need each wax bar to match the length L of the cavity. Originally making the long dimension of the mold equal to L, we found that upon cooling shrinkage at each end reduced the length of the wax by about 1%. We solved this problem by appropriately lengthening the mold with aluminum sheet-metal shims. We poured the wax into the extended mold; after cooling, we removed the shims and scraped the wax ends until they ended up flush with the ends of the aluminum bars and, hence with L for the cavity.

Following the above procedure we produced two wax bars, B_1 with width $w_1 = 18.055(14)$ cm and B_2 with width $w_2 = 19.111(25)$ cm. At a "room" temperature of 19(0.5) °C, their lengths and widths, respectively, fill L and H_2 of the microwave cavity.

E. Measurement of the dielectric constant of wax

We measured the dielectric constant κ_e^w of each wax bar by measuring the set of resonant frequencies of a microwave cavity entirely filled by it. The resonances of a quasi-two-dimensional cavity filled with a medium, here wax, with electric permittivity $\epsilon^w = \kappa_e^w \epsilon_0$ and magnetic permeability $\mu^w = \kappa_m^w \mu_0$, have frequencies given by

$$f = \frac{c}{2\sqrt{\kappa_m^w \kappa_e^w}} \sqrt{\left(\frac{n}{L}\right)^2 + \left(\frac{m}{w}\right)^2}, \tag{37}$$

where c is the speed of light; ϵ_0 and μ_0 are, respectively, the electric permittivity and magnetic permeability of vacuum; n and m are the mode indices; and L and w are, respectively, the length and width of the wax-filled cavity. Assuming, with justification [72], that $\kappa_m^w = 1$, Eq. (37) can be solved for κ_e^w.

We made a wax-filled cavity by pushing the chosen wax bar to one side of the microwave cavity and inserting one of the extra aluminum bars to make a new, temporary fourth side. This bar can move laterally so the width w of this "small" cavity can be made equal to the width of the wax bar being tested. We measure each small-cavity spectrum with the same procedure used for the larger, RS cavity.

To extract κ_e^w for each bar from its corresponding set of resonance frequencies, we need the mode numbers for each resonance. We started with an approximate, tabulated value [[73] Table 6.12] for the dielectric constant of paraffin wax ($\kappa_e^w = 2.30$), calculated the expected resonance frequencies, and then listed them next to their mode numbers n and m. We matched the experimental spectrum to the theoretical spectrum to find the values for n and m for each resonance. We then calculated the dielectric constant for each resonance for further analysis, which included examining if the dielectric constant varies appreciably with frequency. Over the frequency range we covered, 0.5–2.3 GHz, it does not.

However, there are nonrandom, systematic variations for each bar. One that is particularly noteworthy for B_1 is that for fixed m, the largest variation of κ_e^w occurs at low n. Because low-n, low-m wave functions vary more slowly with spatial coordinates (x,y) than high-n, high-m wave functions do, the observed variation could well be a result of less "averaging" in the former case over small spatial inhomogeneities in the solidified wax. The data for B_1 show a systematic decrease in the average value of κ_e^w as n increases; the data for B_2 do not.

Table I summarizes our experimental results. For bars B_1 and B_2 (column 1) and given m (column 2) the values of κ_e^w for N_{id} identified resonance frequencies (column 4) within an n range (column 3) lie in a κ_e^w range shown in column 5 and their mean (standard deviation) is listed in column 6. The average (standard deviation) of the entire B_1 and B_2 data samples are $\kappa_e^w(\mathrm{B}_1) = 2.245(2)$ and $\kappa_e^w(\mathrm{B}_2) = 2.236(5)$, respectively. Based on the two sets of results, we cannot rule out that κ_e^w for the two bars is slightly different. Since each bar was produced from a separate melt of wax, this is not unreasonable. We may combine the measurements for both bars with a worst-case error estimate and quote $\kappa_e^w = 2.236(13)$ between 0.5 and 2.3 GHz.

F. Microwave generation and detection

Figure 5 shows a block diagram of our experimental setup for measuring spectra. A frequency synthesizer (Gigatronics model 1018), which can be controlled via the IEEE-488 (GPIB) interface, operates in steps as small as 1 kHz between 50 MHz and 18.4 GHz and provides microwave power up to 16 mW over the frequency range needed in this experiment, approximately 0.1–2.3 GHz.

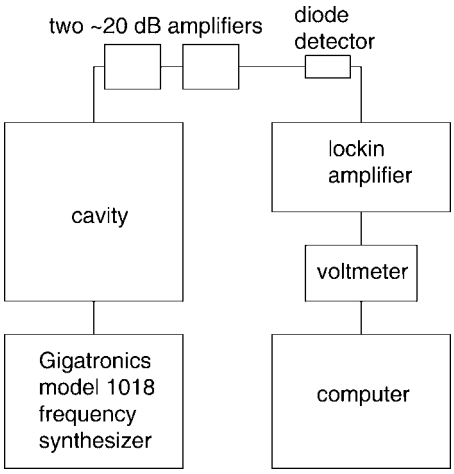

FIG. 5. Block diagram of the experimental setup.

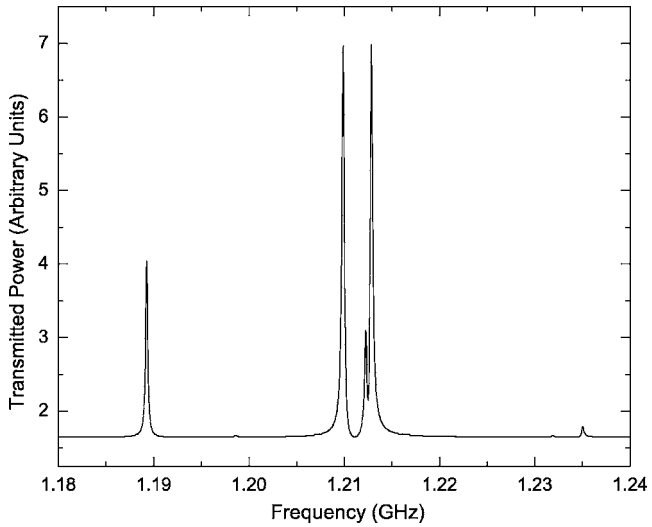

FIG. 6. Portion of a typical microwave spectrum illustrating the resolution of our experiments.

Inserted at a given time into two of the holes drilled into the aluminum-bar sidewalls of the cavity, two antennae ("transmitting" and "receiving") couple power into and out of the cavity. Each one is a magnetic-loop antenna made from a length of UT-141 (3.6 mm outer diameter) semirigid coaxial cable by stripping back a bit of the copper outer (tube) conductor and plastic polymer dielectric, forming a few millimeters long loop from the now exposed copper center wire, and soldering the end of the wire to the outer conductor.

Since the amount of power passed through the cavity is small, typically 60 dB below the incident power even on resonance, we use two cascaded amplifiers to boost the signal from the receiving antenna [74]. Each is made from a Mini-Circuits GAL-3 amplifier chip (name later changed by the manufacturer to GALI-3) soldered into a test board (as is included in the Mini-Circuits "K1-GAL Designers Kit"). The measured power gain for each amplifier exceeds 18 dB between 0.1–2.3 GHz.

A Schottky-diode detector (Hewlett Packard model 8472B) rectifies the amplified microwave signal and produces a voltage approximately proportional to the power from the receiving antenna. A lockin amplifier (Princeton Applied Research model 124A with its final-stage, low-pass filter set to an $RC=30$ ms time constant) with preamplifier (Princeton Applied Research model 117) detects the 1 kHz square-wave amplitude-modulated microwave signal and increases its signal-to-noise ratio by about 10^3, the reference signal being supplied by the synthesizer. A digital multimeter (Fluke model 8840A) reads the voltage signal from the lockin amplifier, and a laboratory computer stores this signal as a function of frequency using the IEEE-488 interface. Individual spectra with up to 3×10^4 data points are recorded at a rate of about two points per second. The control software provides a time delay that allows the frequency and signal to stabilize after each step. Since resonance widths are about 0.3 MHz, we usually choose a frequency step of 0.05 MHz to resolve them. Figure 6 shows a portion of a typical individual spectrum.

To obtain a complete spectrum from the lowest resonance to the highest one that can still be resolved cleanly, we typically record for each cavity configuration and later analyze 10-20 individual spectra taken with different antenna placements and frequency ranges.

V. EXPERIMENTAL SPECTRA: CHARACTERIZATION AND COMPLETENESS

Implementing the movable-bar scheme discussed in Sec. III B 2, we collected a total of four microwave spectra in the frequency range $0<f<2.3$ GHz. Combining data sets obtained with many different antenna placements (see Secs. IV C, IV F, and V D) for a given configuration of the wax bars, each measured spectrum included approximately 210 resonances.

We measured two microwave spectra in the bars-apart configuration [Fig. 2(b)], called "A1" and "A2," respectively, and two in the bars-together configuration [Fig. 2(a)], called "T1" and "T2," respectively. Table II lists the placements of the wax bars for each spectrum.

Although each raw data set contains more than 200 resonances, we noticed early in the data-analysis stage that even a single missing, or spurious, extra resonance, makes it impossible to extract the RS correction from our experimental

TABLE II. Bar placements $[a,b,c,d$, see Fig. 2(b), columns 2–5] for the four experimental spectra (A1, A2, T1, T2, first column) used to measure the RS correction. Each spectrum must contain a complete set of resonances $f_{a,n}^{(\mathrm{expt})}$, $1\leqslant n\leqslant n_a^{(c)}$, where each $n_a^{(c)}$ (sixth column), $a\in\{A1,A2,T1,T2\}$, refers to the end point of the respective complete set of resonances.

Label	a (cm)	b (cm)	c (cm)	d (cm)	$n_a^{(c)}$
A1	17.0	35.0	48.3	67.3	153
A2	15.0	33.0	44.5	63.5	152
T1	15.7	33.7	33.7	52.7	158
T2	22.4	40.4	40.4	59.4	182

data. This means that for valid results, it is crucial that each spectrum be "clean," i.e., free of any missing or extra resonances.

The requirement of spectral completeness distinguishes our experiments from experimental investigations of the statistical properties of experimental spectra [14,60,75]; there one can typically afford to miss up to 5% of the measured resonances with little impact on the experimentally determined statistical properties. Thus spectral completeness, a relatively minor issue in related experimental microwave spectroscopy work [14,60,75], is a central issue in our work.

Given the stringent requirements on spectral completeness in our experiments, we discuss in this section the various methods we used to identify the longest stretch $f_{a,n}^{(\mathrm{expt})}$, $1 \leqslant n \leqslant n_a^{(c)}$ of experimentally measured resonances $f_{a,n}^{(\mathrm{expt})}$, $a \in \{A1, A2, T1, T2\}$ that are certified complete for each data set a. In other words we seek the largest possible completeness cutoff $n_a^{(c)}$ for which all experimentally measured resonances $f_{a,n}^{(\mathrm{expt})}$ with $n \leqslant n_a^{(c)}$ form a complete sequence of states.

A. Staircase method

As a first check we compared the staircase function for each spectrum with the Weyl formula for our cavity. Since the small RS term (26) contributes much less than one level to the Weyl formula over our experimental frequency range, we used $\bar{N}(f)$, defined in Eq. (23), suitably adapted for two wax bars, but without the RS term (26), as a guide to determine where missing or spurious levels might be. To this end we investigated the function

$$J_a(f) = \int_0^f [N_a^{(\mathrm{expt})}(f') - \bar{N}(f')]df', \tag{38}$$

where $N_a^{(\mathrm{expt})}(f)$ is the staircase function for data set a. We found that the frequency average in (38) increases the sensitivity to missing and extra states. If $N_a^{(\mathrm{expt})}(f)$ is complete, we expect that $J_a(f)$ is near zero. Indeed, plotting $J_a(f)$ in the frequency interval $0.5 < f < 2.0$ GHz showed that for all four data sets $J_a(f)$ fluctuates in the range -0.1 GHz states $< J_a(f) < 0.3$ GHz states. As an example, Fig. 7 (full line) shows $J_{A1}(f)$. According to Eq. (38), a missing state results in a "veering off" of the $J_a(f)$ function with a slope of -1 states. To illustrate the effect of a missing state on the J function defined in (38), we deleted resonance number 38 ($f_{A1,38}^{(\mathrm{expt})} \approx 1$ GHz) in data set A1 and show the corresponding J function as the dashed line in Fig. 7. The resulting veering off with a slope of about -1 states, starting at around 1 GHz, is clearly visible. At a frequency of about 2 GHz this slope becomes even steeper, indicating that, in addition to the artificially deleted resonance at about 1 GHz, the experimental spectrum is missing resonance(s) around 2 GHz.

All four data sets A1, A2, T1 and T2 show the veering-off phenomenon around 2 GHz (for A1 see Fig. 7), indicating that our data sets are indeed incomplete above some $n_a^{(c)} < 210$. While it is difficult to pinpoint the onset of the veering-off phenomenon because of the (expected) fluctuations in $J_a(f)$ (see Fig. 7), it is not hard to identify its asymptotic regime, a smooth line with slope ≈ -1 states, changing to ≈ -2 states if a second state is missing. Identifying the onset of the asymptotic regime in $J_a(f)$, we obtain the following conservative estimates for the completeness cutoff $n_a^{(c)}$: $n_{A1}^{(c)} < 185$, $n_{A2}^{(c)} < 184$, $n_{T1}^{(c)} < 176$, and $n_{T2}^{(c)} < 191$. That we did not observe a veering-off phenomenon with slope +1 states means that none of the four spectra contains a state in excess of what is predicted by $\bar{N}(f)$.

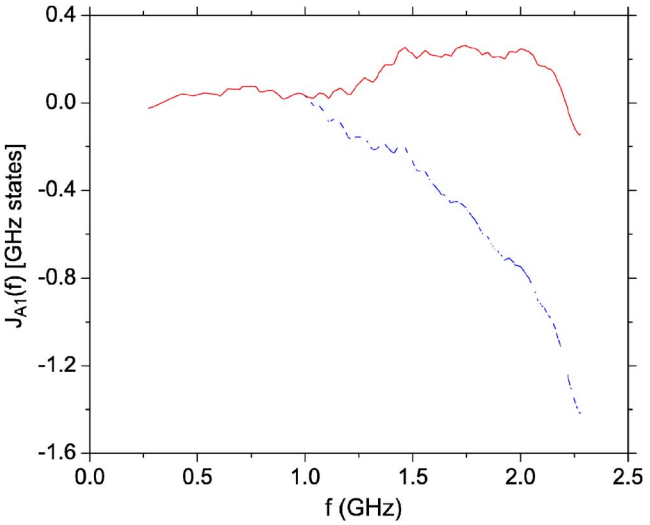

FIG. 7. (Color online) Illustration of the veering-off phenomenon used to assess completeness of our spectra. Full line: The function $J_{A1}(f)$ (see text) for the experimental spectrum A1. Dashed line: Deleting a resonance level around 1 GHz in the experimental spectrum produces an immediate and dramatic effect in the integrated difference signal $J_{A1}(f)$.

Unfortunately, as illustrated in Fig. 7, the staircase method is not very accurate. Moreover, it is insensitive to a scenario in which a missing state at frequency f_1 gets "compensated" by a spurious, extra state at frequency f_2 with $|f_1 - f_2| \ll 1$ GHz. This scenario does indeed occur in our spectra and necessitates a more serious pruning of the data sets than was afforded by the staircase method. A more accurate method is also needed because the staircase method does not yield the precise locations of missing states. In fact, taking the effect of fluctuations into account, we judge that the above conservative estimates for $n_a^{(c)}$ may overestimate the exact location of the first missing resonance by as many as 40 states. This is unacceptable.

B. Spectral comparisons: Difference method

The next, more accurate check compares experimental spectra with numerical spectra generated by computational simulation of the dielectric-loaded cavity. We investigate the quantity

$$K_{a,n} = f_{a,n}^{(\mathrm{expt})} - f_{a,n}^{(\mathrm{num})}, \tag{39}$$

where the first and second terms on the RHS of Eq. (39) are, respectively, measured and numerically calculated resonance frequencies. The problem area in each data set is easily iden-

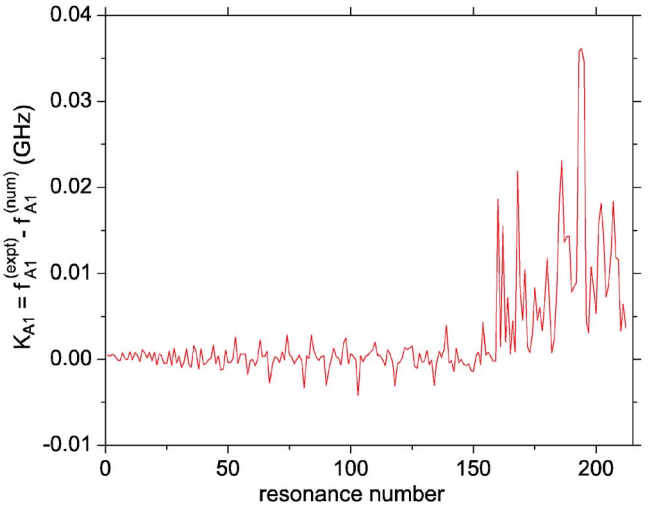

FIG. 8. (Color online) Veering-off phenomenon in the A1 spectrum around resonance number 160 as measured by the function K_{A1} indicating a missing state in the measured A1 spectrum which occurs at a level number smaller than about 160.

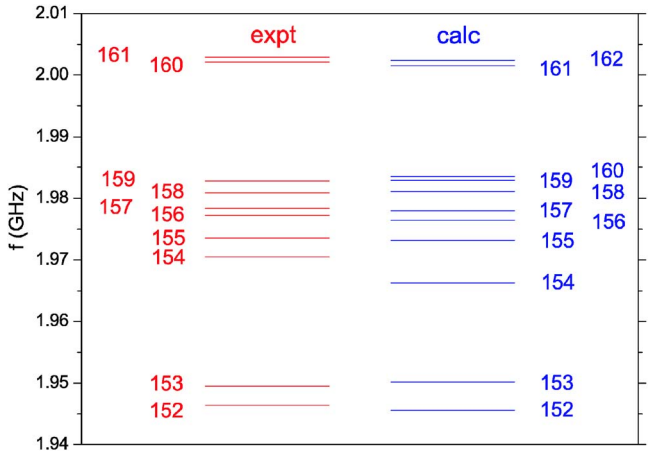

FIG. 9. (Color online) Comparison between the experimental spectrum A1 (left ladder) and its numerical simulation (right ladder).

tified visually. We find that about the first 150 resonances in each of the four data sets produce a mildly fluctuating signal with an amplitude on the order of less than ±0.005 GHz. A sudden jump by a factor of three to four in the amplitude of fluctuations indicates a missing resonance or an extra resonance. Figure 8 illustrates this for spectrum A1, showing that it is patently obvious that there is a problem near resonance number 160. We found that the difference method is much more accurate than the staircase method. On the basis of the difference method, and with an accuracy of about ±10 states, we are sure that a problem occurs in each spectrum as follows: at $n \approx 160$ for A1; at $n \approx 160$ for A2; at $n \approx 165$ for T1; and at $n \approx 185$ for T2. Having zoomed in on the problem areas, we are now ready for a visual state-by-state comparison of the experimental spectra with the numerically simulated spectra. Our goal is to obtain exact values for the completeness cutoffs $n_a^{(c)}$.

C. Visual state-by-state comparisons

Figure 9 is an example of a side-by-side comparison of experimental *A*1 and numerical *A*1 spectra over the frequency range 1.94–2.01 GHz. Experimental "energy levels" are on the left; the numerical resonances are on the right. Ordinal numbers count the levels above the ground state, level number 1. Figure 9 shows that the levels are clustered. There is a one-to-one correspondence of clusters and some rough correspondence of levels within clusters. The clustering phenomenon observed in our experiments is well known in a different context in atomic and nuclear physics, where the clusters are called "shells." Up to level number 153 we find a one-to-one correspondence between experimental and numerical clusters with precisely the same number of levels in corresponding clusters. Therefore we assert that the experimental A1 spectrum is complete up to at least resonance number 153. Focusing now on the cluster between frequencies 1.96 and 1.99 GHz, we see that the experimental cluster contains six levels while the numerical cluster contains seven levels. Assuming that the numerical spectrum is complete (see discussion of this point in Sec. V D below) an experimental resonance must be missing in this cluster of levels. One is tempted to say that the missing experimental resonance is one of the near degenerate doublet of resonances (numbers 159 and 160) predicted by the numerical calculations, but it could also be a problem around resonance number 154.

A comparison between the spatial structures of wave functions might resolve this issue, but since we did not measure the wave functions experimentally (see, e.g., [60]), we cannot identify with certainty the missing experimental resonance in the 1.96–1.99 GHz cluster. To be on the safe side, we assert with confidence that our measured A1 spectrum is complete up to and including resonance number 153, which means $n_{A1}^{(c)} = 153$. A similar analysis of the remaining three data sets yields $n_{A2}^{(c)} = 152$, $n_{T1}^{(c)} = 158$, $n_{T2}^{(c)} = 182$. These values are summarized in column six of Table II. We conclude that up to the $n_a^{(c)}$ values stated our experimental spectra are complete beyond a reasonable doubt.

D. Spectral completeness: Discussion

It is impossible on the basis of experiment alone for one to assert completeness of an unfamiliar, unknown spectrum. One may miss a resonance simply because one cannot probe all points inside a cavity with an antenna. Given any finite set of antenna placements, especially in the short-wavelength limit, one can always imagine a state whose nodal lines or surfaces (loci of zero field) lie along the chosen antenna placements. Therefore additional information is required, either from analytical or numerical calculations. Section V C above showed how we are able to pinpoint missing states by comparing with numerical calculations.

Based on numerical techniques alone, it is equally impossible to assert completeness of a numerical spectrum. Numerical techniques require the implementation of search protocols. No matter how small the step size, one may still miss

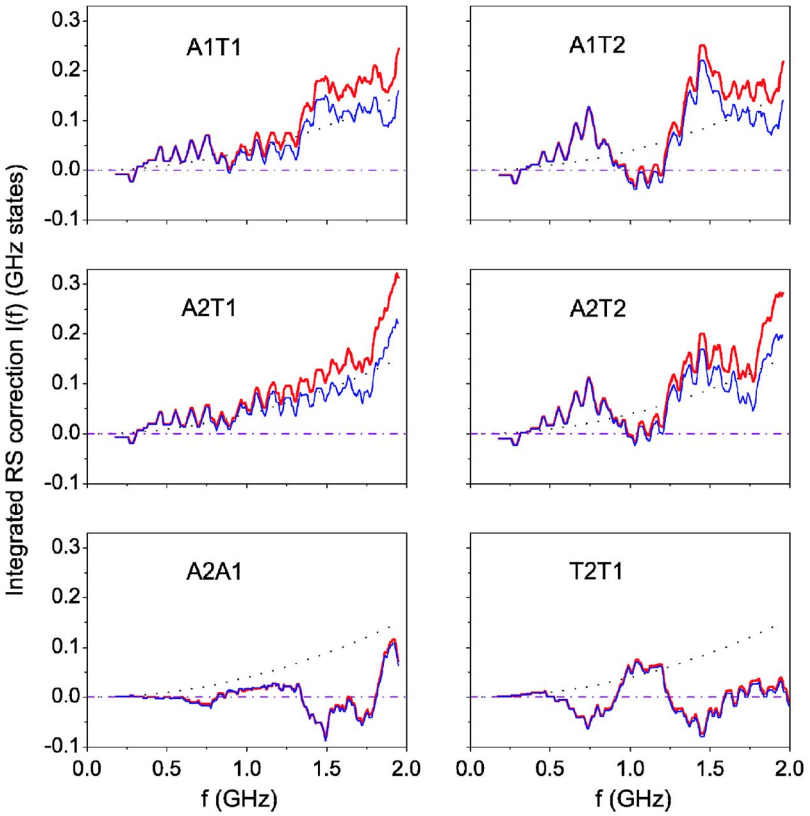

FIG. 10. (Color online) The integrated differences $I_{ab}(f)=\int_0^f[N_a(f')-N_b(f')]df'$ between staircase functions $N_{a,b}(f)$ corresponding to two different bar configurations $a,b\in A1,A2,T1,T2$. The six panels show the integrated difference for the six nontrivial combinations ab=A1T1, A1T2, A2T1, A2T2, A2A1, T2T1, respectively. Heavy full lines: Experimental results. Thin full lines: Numerical simulations. Dotted lines: Analytical prediction $\bar{I}^{(ana)}(f)$. Dash-dotted line: $I=0$ baseline. The first four panels, corresponding to the four possible differences between bars-apart and bars-together configurations, show a RS signal that is consistent with the numerical calculations and the analytical prediction. The bottom two panels (A2A1 and T2T1) are null tests; in both cases the experimental (heavy full) and numerical (thin full) curves lie nearly on top of each other over the whole range.

a resonance. This is obvious in a case of accidental, exact degeneracy, which one can never rule out. Only analytical techniques have the advantage that they never "miss a state."

We used analytical techniques in the following way to certify completeness of each numerical spectrum up to some frequency. We started the calculations with an empty cavity (no wax bars) and compared the numerical spectrum to the analytically known spectrum. We found it to be complete. Then we "turned on" the wax bars by slowly raising the dielectric constant of the wax bars from $\kappa_e=1$ to κ_e^w, which allows us to follow every resonance, quasi adiabatically, from the no-wax case to the full-wax case to certify that the numerical spectra are complete. Thus do we use the numerical spectra as a gauge for the experimental spectra. To certify completeness of experimental spectra both analytical and numerical methods must be applied.

VI. THE RAY-SPLITTING CORRECTION

Having established in Sec. V completeness of the four experimental spectra up to level numbers listed in Table II, we are ready to extract from them the experimental RS correction. Section VI A presents these results. Since our experimental protocols involve wax bars in apart (A) and together (T) configurations, we address in Sec. VI B "what is apart and what is together." Experimental RS results are systematically shifted with respect to the numerical results and analytical expectations. We have considered two mechanisms that could explain this shift: temperature and the top lid of the cavity being slightly buckled (nonplanar). Section VI C discusses and rules out temperature variations as a possible candidate. Section VI D discusses lid buckling and shows that it is the likely explanation for the observed shifts.

A. Extraction of the ray-splitting correction from experimental data: Results

Section III B motivated and described our method for extracting the RS correction from the experimental data. It is based on the investigation of the integrated differences $I^{(expt)}(f)$ [see Eq. (35)] between apart and together experimental spectra.

1. Apart-together comparisons

Figure 10 compares $I^{(expt)}(f)$ (heavy full lines) with the analytical predictions [see Eq. (36)] $\bar{I}^{(ana)}(f)$ (dotted lines) and with numerical results $I^{(num)}(f)$ (thin full lines) that are discussed below. The top four panels show the integrated difference between bars-apart and bars-together staircase functions, where, e.g., "A1T1" labels the integrated difference curve of staircase functions from cavity configurations A1 and T1. Given the $n_a^{(c)}$ cutoffs listed in Table II, the integrated differences are based on 153 resonances for A1T1 and A1T2 and on 152 resonances for A2T1 and A2T2.

All four experimental curves (heavy full lines) exhibit "fine oscillations" (hereafter, oscillations) with roughly 0.1 GHz spacing as well as "coarse undulations" (hereafter, undulations) over a wider frequency range. We emphasize that the reasonable agreement between the experimental curves $I^{(expt)}(f)$ and the numerical curves $I^{(num)}(f)$ includes both the oscillations and undulations; moreover, we find both

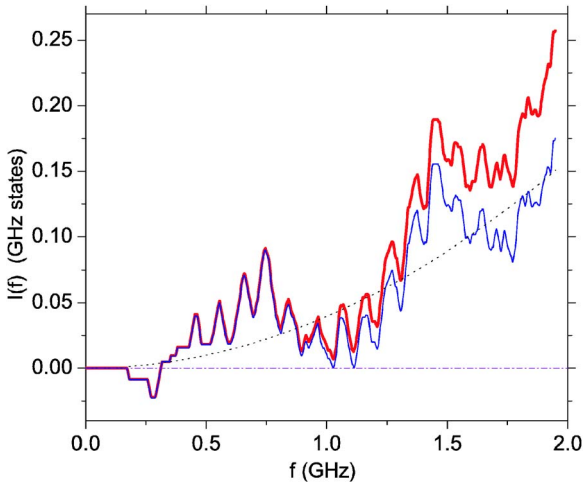

FIG. 11. (Color online) Integrated difference obtained as the average of the top four panels in Fig. 10 (heavy full line). Also shown is the numerical simulation of the average integrated difference (thin full line), the analytical prediction for the integrated difference $\bar{I}^{(\mathrm{ana})}(f)$ (dotted line), and the $I=0$ baseline (dash-dotted line). The reason for the systematic shift upwards of the experimental results with respect to the numerical simulations and the analytical prediction is explained in Sec. VI.

are reproducible when the wax bars are moved by a small amount (0.5 mm). They are robust "detail phenomena" that must be explained. Section X does this.

2. Null tests: Apart-apart and together-together comparisons

The bottom two panels in Fig. 10 show crucial null tests, viz., the integrated bars-apart–bars-apart difference for A2A1 (based on 152 resonances) and the integrated bars-together–bars-together difference for T2T1 (based on 158 resonances). Again, we emphasize that in these null tests, the oscillations are strongly suppressed compared to the four apart-together cases, whereas the undulations are not. Section X explains both the former's suppression and the latter's lack of suppression.

Both experimental null tests meet the challenge: Each is close to zero. The net area under each experimental null-test curve is less than 6% of the area under $\bar{I}^{(\mathrm{ana})}(f)$. Moreover, there is excellent agreement, including the suppressed oscillations and the omnipresent undulations, between each experimental null-test curve and its numerically simulated counterpart.

3. Comparisons of averages and the systematic shift

Figure 11 shows the average (heavy full line) of the top four panels in Fig. 10 along with the corresponding numerical curve (thin full line) and the analytical curve $\bar{I}^{(\mathrm{ana})}(f)$ (smooth dotted line). The averaging barely affects the oscillations present in Fig. 10, though it does reduce the undulations somewhat and gives better agreement with the analytical and averaged-numerical curves. Note, however, that above about 1.5 GHz the undulating experimental curve $I^{(\mathrm{expt})}(f)$ rises systematically above the analytical curve $\bar{I}^{(\mathrm{ana})}\times(f)$. This shift notwithstanding, there is no doubt that our experiment is sensitive to the RS correction and that the observed RS signal is consistent with the analytical expectation $\bar{I}^{(\mathrm{ana})}(f)$, thus confirming experimentally the existence of a universal RS correction to Weyl's law in the presence of sharp interfaces.

To obtain more insight into the nature and magnitude of the shift of the experimental RS signal, we computed the integrated differences $I^{(\mathrm{num})}(f)$ based on the numerical A1, A2, T1, and T2 spectra. The results are shown as the thin full lines in Figs. 10 and 11. Up to about 1 GHz $I^{(\mathrm{expt})}(f)$ and $I^{(\mathrm{num})}(f)$ are practically identical, whereas for higher frequencies $I^{(\mathrm{expt})}(f)$ is systematically higher than $I^{(\mathrm{num})}(f)$. Even with the shift, both curves have virtually identical patterns of oscillations and undulations.

To investigate the cause of the upward experimental shift, we looked at the difference

$$D(f) = I^{(\mathrm{expt})}(f) - I^{(\mathrm{num})}(f) \tag{40}$$

and found it to behave like f^3. Since according to Eq. (24) the area term is $\sim f^2$ its integral is $\sim f^3$. Therefore the observed f^3 behavior of $D(f)$ is consistent with a change in the area term between the apart and together configurations. Perhaps this resulted from a real mechanical change in the cavity dimensions, as discussed in Sec. VI C, or some other mechanism that *mimics* a change in area, as discussed in Sec. VI D. Therefore we attribute the observed shift of $I^{(\mathrm{expt})}(f)$ to a change in "effective area" between apart and together configurations.

The bottom two panels of Fig. 10, i.e., the null tests, support this idea: there is negligible difference between $I^{(\mathrm{expt})}(f)$ and $I^{(\mathrm{num})}(f)$ in both cases. This means that for like-with-like comparisons, either apart-apart or together-together, area and perimeter terms indeed cancel, resulting in the satisfactory null tests. Since, perforce, the numerical calculations conserve the area and the perimeter terms exactly, the observed f^3 dependence of $D(f)$ in the top four panels of Fig. 10 (and their average shown in Fig. 11), can only be explained by some systematic effect that occurs when changing between apart and together configurations. Since the sidewalls of our cavity are tightly bolted together, and since the bolts are not undone between configuration changes, it is impossible that the change in effective area is due to changes in transverse (length and width) cavity dimensions introduced when changing the placement of the wax bars within the cavity. However, changes in the cavity dimensions due to temperature do indeed occur. Their influence is discussed in Sec. VI C and found to be negligible.

However, one of the suprises of this experiment is the extraordinary sensitivity of the integrated difference to slight buckling of the top lid of the cavity. This effect is discussed in Sec. VI D and found to be consistent with the observed shifts in $I^{(\mathrm{expt})}(f)$.

4. Clipping of oscillations

In both Fig. 10 and Fig. 11 the maxima of the oscillations appear "clipped." We checked that the resulting "plateaus" are not due to an insufficiently dense plotting mesh; it is a

real effect that comes from subtracting two staircase functions. Since the staircases are piecewise-constant functions, so, too, is their difference $\Delta N(f)$. Moreover, since the two staircase functions differ only by the small RS correction, there are many frequency intervals within which $\Delta N(f)$ is zero. In such intervals the integral over $\Delta N(f)$, $I^{(\mathrm{expt})}(f)$, is constant. This explains the clipping seen in Figs. 10 and 11.

B. What is apart versus what is together

Ideally, in the limit of zero wavelength, any finite gap between the wax bars would qualify as apart, while together would require contact everywhere along the interface in question. Since the wavelength in our experiments ranges from 15 cm to 2 m in air, we must be careful to specify the present meanings of apart and together: At a wavelength of 15 cm a gap of, say, 1 cm may not be resolved and may thereby qualify as a together configuration even though, to the eyeball, the bars are apart. This argument cuts both ways. On the one hand we must ensure that at experimental wavelengths the wax bars are far enough apart to qualify as apart. On the other hand the finite-wavelength effect helps us because residual surface imperfections in the wax bars mean that even in the "together" configuration, localized gaps of, say, 1 mm remain. While at wavelengths shorter than 1 mm this would be a serious situation, it may not matter in our experiments, where imperfection gaps are far smaller than all wavelengths we use.

To address this question quantitatively, we computed the RS correction as a function of a uniform gap g between the wax bars for 201 different apart configurations labeled Aj, where the index j runs from −100 to +100. The bar placements a_j, b_j, c_j, and d_j for bar configurations Aj are defined as $a_j=a_{\mathrm{A1}}+js_1$, $b_j=b_{\mathrm{A1}}+js_1$, $c_j=c_{\mathrm{A1}}+js_2$, $d_j=d_{\mathrm{A1}}+js_2$, where $s_1=(a_{\mathrm{T1}}-a_{\mathrm{A1}})/100$, $s_2=(c_{\mathrm{T1}}-c_{\mathrm{A1}})/100$, and a_{A1}, etc., are listed in Table II. As j runs from −100 to +100, the gap between the bars in the corresponding apart configurations Aj decreases from an initial gap of 26.6 cm at $j=-100$ to a gap of 0 cm (A100≡T1). For each Aj we computed 153 resonances and computed the integrated differences $I_j(f)$ between the staircase functions $N_{\mathrm{A}j}(f)$ and $N_{\mathrm{T1}}(f)$. Since according to (26) $\bar{N}_{\mathrm{RS}}(f)$ is linear in f, we expect each $I_j(f)$ to be quadratic in f on average (see also Figs. 10 and 11). Therefore we characterize the RS correction for each gap g_j by fitting a quadratic function in f to $I_j(f)$ and extracting the corresponding ν_j, which, according to Eq. (26), uniquely characterizes the RS correction.

The result is shown as the full line in Fig. 12. The horizontal line in Fig. 12 is at the value of ν that, according to Eq. (27), is expected for $\nu_0=0.024\,64$, i.e., for wax bars with $\kappa_e^w=2.236$ (see also Fig. 3). Since we used T1 as the reference spectrum for the extraction of the RS correction in the AjT1 configurations, the RS correction is trivially zero at $g=0$. As the gap between the wax bars increases, the RS correction starts to rise, reaches the value ν_0 at a gap of about 5 cm, overshoots, oscillates, and then drops precipitously for gaps larger than about 25 cm.

For large gaps the right-hand bar approaches the right-hand wall of the cavity. In fact, at $j=-100$ the gap is 26.6 cm wide, and the right-hand wax bar is only 7.9 mm from the right-hand cavity wall. This changes the metallic boundary condition to a wax-metal boundary condition. Our derivation of the Weyl formulas (23)–(29), assumed that the wax bars are sufficiently far away to consider the left and right-hand walls of our cavity to be *metallic* walls. A wax-metal boundary condition produces a different perimeter term that, however, has the same frequency dependence as the RS correction. Thus, when one, or both, of the wax bars comes too close to the left- or the right-hand cavity walls, the wax-metal perimeter term appears as an effective RS term. This explains the precipitous drop in the RS signal in Fig. 12 for large gaps g. We do not yet know what causes the sharp rise of the RS signal before that drop.

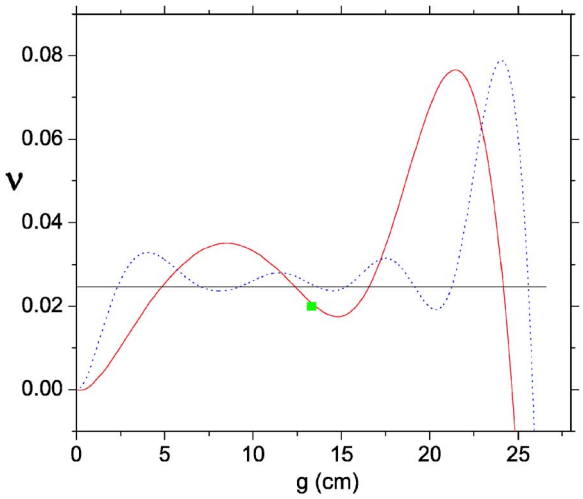

FIG. 12. (Color online) RS strength ν [see Eq. (26)] as a function of the distance (proximity) between wax bars computed on the basis of 150 resonances (full line) and 500 resonances (dashed line). The plot symbol marks the bar separation in one of our experiments.

The filled-square plot symbol in Fig. 12 marks the value of ν for $g=13.3$ cm, which is the value of g for our A1 data set. We see that at this gap the RS signal obtained from the A1T1 configuration happens to lie close to ν_0.

Figure 12 also shows the result of a calculation where the RS correction is computed on the basis of 500 resonances. As expected, since more resonances means shorter wavelength, the RS signal rises more steeply, and while still oscillating, stays more closely to ν_0.

Figure 12 allows us to give a definitive answer to "What is apart?" and "What is together?" Figure 12 shows that for 153 resonances the borderline between apart and together configurations is a gap of 5 cm. Figure 12 also shows that with good accuracy gaps smaller than 5 mm count as "together." Thus Fig. 12 confirms that at the wavelengths used in our experiments we need not worry about wax-surface imperfections that prevent the wax bars from making perfect contact in together configurations. Figure 12 shows that a residual gap of, say, 1 mm may be interpreted as together with excellent accuracy and that apart configurations start with a gap of about 5 cm.

However, as discussed above, larger gaps in our cavity do not necessarily generate better apart configurations, since for

gaps larger than about 17 cm we encounter the problem with the wax-metal boundary condition. Therefore, acceptable apart configurations in our experiments are in the range $g=5-17.5$ cm. The gaps for A1 and A2, respectively 13.3 cm and 11.5 cm, are both within this range. This validates our choice of gaps for the experimental apart configurations.

C. Temperature

For the movable-bar scheme to work it is essential that the cavity geometry be the same during the measurement of spectra for *all* configurations of the wax bars. This makes temperature fluctuations in the laboratory be a real concern because thermal expansion or contraction change the cavity dimensions. While we used an air-conditioned room, which allowed us to keep the temperature constant within ±0.5 °C, the setup, itself, was not temperature controlled.

A rise (fall) in temperature results in thermal expansion (contraction) of both the aluminum cavity sidewalls and the wax bars, which, together, cause changes in the area, perimeter, and RS terms in the mean staircase function (23). Since our method is based on the cancellation of area and perimeter terms, a change of these terms during the measurement of spectra might have disastrous consequences.

Let us compute the effect of temperature variations on the size of $I^{(\mathrm{expt})}(f)$ at $f=2$ GHz. Assume that an apart measurement was taken at temperature $T+\Delta T$ and a together measurement at temperature T. An estimate for the temperature-induced error in $I^{(\mathrm{expt})}(f)$ is

$$\Delta I(f) = \int_0^f [\bar{N}(f', T+\Delta T) - \bar{N}(f', T)]df', \tag{41}$$

where $\bar{N}(f', T)$ is the average staircase function (23) at frequency f' and temperature T. To simplify the argument we approximate $\bar{N}(f', T)$ by $\bar{N}_A(f', T)$, the leading term in (23). This approximation results in $\Delta I(f) \sim f^3$, which is consistent with our observation discussed in Sec. VI A 3 that $D(f)$ [see Eq. (40)], is proportional to f^3. Thus, we obtain

$$\Delta I(f) = \frac{\pi}{3c^2}\Delta A f^3, \tag{42}$$

where

$$\Delta A = A_0(T+\Delta T) + \kappa_e^w(T+\Delta T)A_{\mathrm{bars}}(T+\Delta T) - [A_0(T) + \kappa_e^w(T)A_{\mathrm{bars}}(T)] \tag{43}$$

is an estimate of the "effective area" discussed in Sec. VI A 3.

To evaluate Eq. (43) we need the (linear) thermal expansion coefficients α_{alum} and α_{wax} for aluminum and wax, respectively. We use [76]

$$\alpha_{\mathrm{alum}} = 23 \times 10^{-6}\ \mathrm{K}^{-1}, \quad \alpha_{\mathrm{wax}} = 195 \times 10^{-6}\ \mathrm{K}^{-1}, \tag{44}$$

respectively. Noting that

$$A_0(T) = A_{\mathrm{cav}}(T) - A_{\mathrm{bars}}(T), \tag{45}$$

where $A_{\mathrm{cav}}(T)$ and $A_{\mathrm{bars}}(T)$ are, at temperature T, the respective areas of the cavity and the wax bars, we obtain a rough estimate for the order of magnitude of ΔA by assuming that $\kappa_e^w = 2.236$ is constant over the temperature range ΔT. To first order in α_{alum} and α_{wax} we obtain

$$\Delta A = 2.1 \times 10^{-4}\left(\frac{\mathrm{m}^2}{\mathrm{K}}\right)\Delta T. \tag{46}$$

Inserting this result into Eq. (42) we obtain

$$\Delta I(f) = 2.4 \times 10^{-3}[f\ (\mathrm{GHz})]^3\left(\frac{\mathrm{GHz\ states}}{\mathrm{K}}\right)\Delta T. \tag{47}$$

According to Fig. 10, $I^{(\mathrm{expt})}(f)$ amounts to about 0.15 GHz states at $f=2$ GHz. Therefore, for $f=2$ GHz and $\Delta T=5$ K, we obtain

$$\frac{\Delta I(2\ \mathrm{GHz}, \Delta T = 5\ \mathrm{K})}{I^{(\mathrm{expt})}(f)} = 0.64. \tag{48}$$

We see that a temperature difference of $\Delta T=5$ K between measurements with bars apart versus bars together results in a relative error of 64% for the RS correction at 2 GHz. The relative error decreases to less than 10% for $\Delta T=0.5$ K. Based on these estimates, we made sure that the temperature during the measurements was kept constant at (19±0.5) °C during the several weeks needed to take the (final) data for the A1, A2, T1, T2 configurations. Since the shift of $I^{(\mathrm{expt})}(f)$ with respect to $\bar{I}^{(\mathrm{ana})}(f)$ discussed in Sec. VI A is much larger than 10%, temperature fluctuations in our laboratory cannot explain it.

D. Lid buckling

As discussed in Sec. VI A 3 the difference between the experimental and numerical integrated differences shows an f^3 dependence. According to Eq. (24) the frequency-integrated area term is also proportional to f^3. Thus, the shift of the experimental RS signal $I^{(\mathrm{expt})}(f)$ above $I^{(\mathrm{num})}(f)$ could be explained by a change in effective area ΔA when changing an apart configuration to a together configuration. Since $D(f)$ is positive, ΔA is positive, which means that the apart configurations (A1 and A2) have larger effective area than the together configurations (T1 and T2). In other words, ΔA corresponds to an apparent "missing area" when comparing together and apart configurations.

We now compute the magnitude of ΔA for the case A1T1. Integrating (24) gives

$$D(f) = \frac{\pi}{3c^2}\Delta A f^3, \tag{49}$$

from which we obtain $\Delta A = 1073\ \mathrm{mm}^2$, using our estimate of $D(f=2\ \mathrm{GHz}) = 0.1$ GHz states from the A1T1 panel in Fig. 10.

To test our estimate of the missing area we numerically fitted the experimental spectra, A1, A2, T1, T2 to "optimized" cavities in the following way. We solved the Helmholtz equation for each of the cavity geometries specified in Table II, keeping the length $L=0.960\,48$ m fixed, but optimizing the width e of the numerical cavity. The optimization was done by computing the integrated difference between the

staircase function for experimental spectra and the numerically obtained staircase function as a function of e. Visually inspecting the resulting integrated difference curves, we find the optimal values of e that best reproduce the experimental spectra. We find $e_{A1}^{(opt)}=0.8266$ m, $e_{A2}^{(opt)}=0.8268$ m, $e_{T1}^{(opt)}=0.8255$ m, $e_{T2}^{(opt)}=0.8257$ m. To judge the quality of the fits at the optimal e values quoted above, we note that the absolute value of the integrated difference between the experimental staircases and the staircases of the numerical spectra of the optimized cavities is less than 6×10^{-3} GHz states in each of the four cases. This is on the order of, or less than, one-tenth the RS signal of our null tests shown in the bottom panels of Fig. 10. Focusing again on the A1T1 case we see that the difference in width between the respective optimized cavities is 1.1 mm. At a length $L=0.960\,48$ m of the respective cavities, this amounts to 1057 mm^2, a value which compares favorably with the above estimate $\Delta A=1073$ mm^2 of the missing area extracted directly from the RS signal shown in the A1T1 panel of Fig. 10.

The question then becomes what caused the missing area? To answer it we considered the effects of (i) temperature (ruled out in Sec. VI C above), (ii) air humidity, (iii) mechanical disturbances of the cavity geometry when changing wax bar positions, and (iv) the antenna holes, the number of which are (partially) covered or uncovered varying by one or two according to the apart and together configuration being used. Finding that all four candidates listed above produce effective areas that are too small to explain missing areas on the order of 10^3 mm^2, we rule them out.

We are left with one possible mechanism, viz., buckling (nonplanarity) of the top lid of the cavity. [Because the lower lid was always laid flat on the steel table (see Sec. IV A), we rule out its being buckled.] As discussed in Sec. IV B, the lids are fairly thin circuit board, and unlike the bottom lid, the top lid was supported from below by (i) the four cavity sidewalls, (ii) the two wax bars, and (iii) 18 plastic spacers each made of a rolled-up spiral of polymer sheet plastic used for overhead transparencies. We carefully cut the spacers to keep their height uniform to 0.13 mm or better and randomly placed them in the air-filled regions. To minimize upward lid buckling, we also placed the four spare aluminum sidewall bars (see Sec. IV C) across the top lid, with their weight supported at their ends, through the top-lid circuit board, by the actual sidewalls of the cavity.

These precautions notwithstanding, there could be local increases or decreases in the distance between the top and bottom lids (or between the top lid and the upper surfaces of the wax bars), causing the cavity to be nonuniform in height. Since a nonuniform cavity height breaks the Q2D-ness of our cavity, it certainly affects the frequencies of the cavity resonances, thereby producing a systematic error in the integrated differences. Let us suggest that the frequency shifts induced by lid buckling can be modeled by a "missing area" and thus explain the upward shifts in the experimental RS signal.

We explicitly tested this hypothesis in the following way. We temporarily mounted a piece of steel box tubing above and across the cavity. The ends of the box tubing were anchored to the steel table on which the cavity sat, but the box tubing could not touch the cavity except for three screws we put into holes tapped into the box tubing. By tightening the screws we could press down on the cavity lid in a controlled way. To prevent "point contacts" that could damage the circuit board, we put a long piece of sheet metal between the screws and the top-lid circuit board; this distributed the pressure from each screw over a larger area. For this test the wax bars were in a bars-apart configuration, and the screws were positioned so that they pressed down in the center of the three air-filled gaps inside the cavity.

We placed a Last Word™ indicator as close as possible to each screw and used them to measure the deflection of the circuit board with 1 mil precision (1 mil=0.001 in. =0.0254 mm). Careful measurements at 2 GHz for lid deflections ranging, in 2 mil steps, from 2 mils to 10 mils, revealed frequency shifts of up to 200 kHz. Careful measurements of lid surface positions without the screws present (unloaded surface) revealed that the cavity lid positions typically varied in a 20 mil range. This means that at 2 GHz, we could encounter typical frequency shifts of about 200 kHz. Most resonances shifted downward in frequency, but some shifted upward by a significantly smaller amount.

Are these shifts consistent with the missing area estimated above? To answer this we recall that the missing area corresponds to a change in optimized cavity width of $\delta e=-1.1$ mm for the A1T1 case we treated as an example. For a crude estimate we use the frequency formula (37) with $\kappa_e=1$ and obtain for the frequency shift δf to first order

$$\delta f_{nm}=-\frac{m^2c^2}{4e^3f_{nm}}\delta e. \tag{50}$$

For $\delta e=-1.1$ mm this amounts to $\delta f\approx200$ kHz at an average mode number of $m\approx3$. Thus the frequency shifts produced by lid buckling are consistent with the frequency shifts predicted by the optimized cavities, which in turn produce optimal representations of the experimental spectra. This shows that lid buckling is capable of producing the needed missing area and, thus, is capable of explaining the observed upward shift in the A1T1 case.

Although our examples focused on the A1T1 case, similar calculations show that the shifts in all remaining cases (A1T2, A2T1, A2T2) could also be explained by lid buckling. Although we did not prove it, our estimates make a strong case for lid buckling as the most likely mechanism for explaining the observed shifts of the RS signal in all cases shown in Figs. 10 and 11.

VII. WAVE-FUNCTION LOCALIZATION

Wave functions for dielectric-loaded cavities show features not found in empty Q2D cavities. Though we did not measure the wave functions (as could be done using, e.g., methods described in [60]) in the cavity loaded with wax bars, they are readily available computationally. For example we computed the first 158 wave functions of the cavity in T1 configuration; see Table II. We used a 2D gray scale to represent the square modulus of each wave function and examined such plots visually. Apart from wave functions that are spread out over the whole cavity, to be called *delocalized*, we

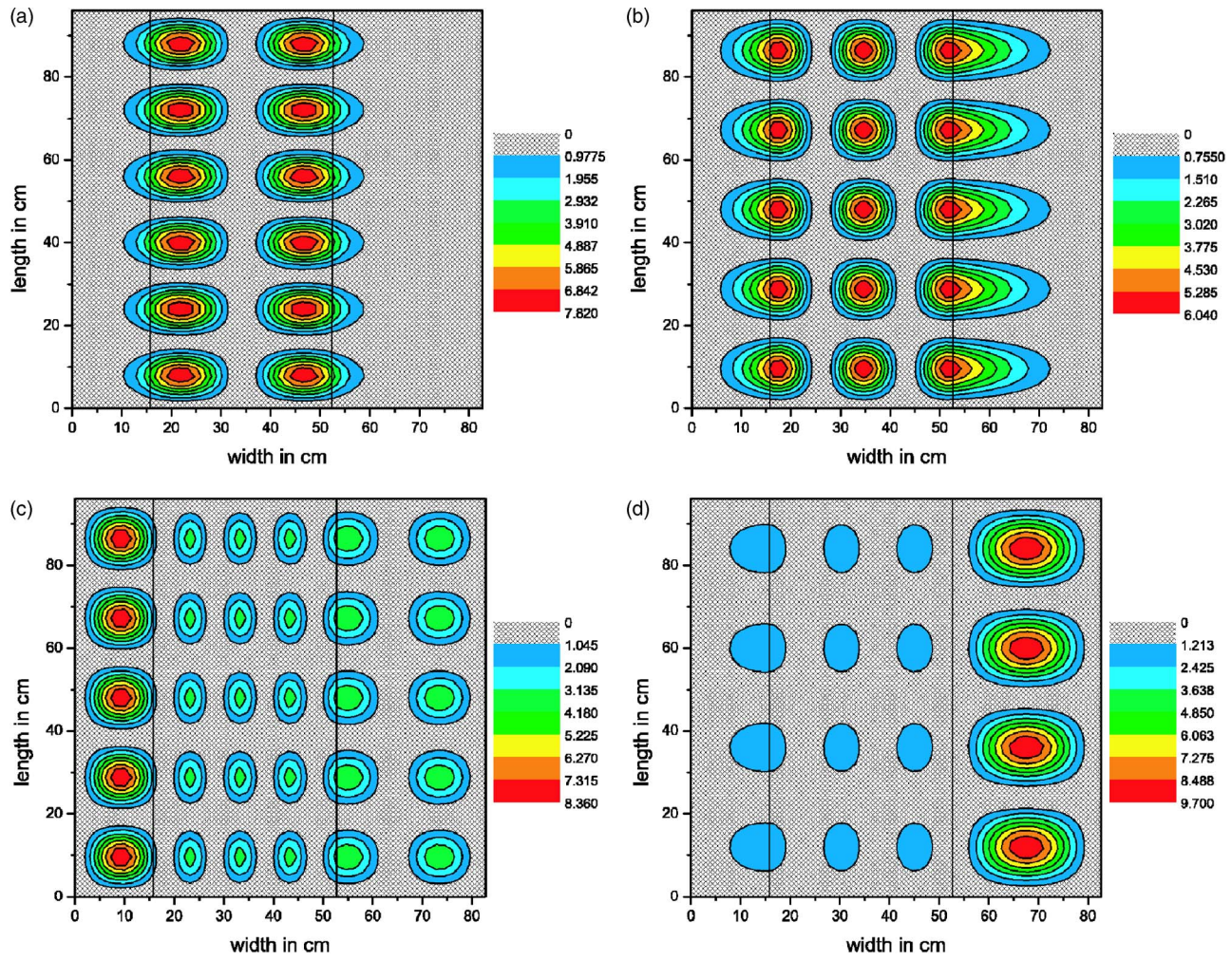

FIG. 13. (Color online) Examples of four types of states encountered in our experiments for the wax bars in T1 configuration. (a) Classically trapped wave function $(m,n)=(2,6)$; (b) hovering wave function $(m,n)=(3,5)$; (c) left-localized wave function $(m,n)=(1,5)$; and (d) right-localized wave function $(m,n)=(1,4)$.

find many types of *localized* wave functions. The lettered panels in Fig. 13 show, respectively, the four basic types for the bars-together cavity (when the L edges of both wax bars are away from the metal sidewalls, as shown in the figure): (a) wave functions that are classically trapped in the wax, to be called *trapped*; (b) wave functions that are trapped in the wax due to non-Newtonian reflections, to be called *hovering*; (c) wave functions that are confined to the space between the left-hand cavity wall and the left edge of the wax, to be called *left localized*; (d) wave functions that are confined to the space between the right-hand cavity wall and the right edge of the wax, to be called *right localized*.

We find it easiest to discuss these wave functions and their structures in the equivalent quantum mechanical picture presented in Sec. II A, for which an electromagnetic mode function at frequency f in the wax-loaded cavity corresponds to the wavefunction of a quantum particle at energy $E=4\pi^2f^2/c^2>0$, the air-filled regions (called *shelf regions* below) correspond to zero potential, the regions filled with wax (called *wax regions* below) correspond to a finite square-well potential of depth $V_0=-(\kappa_e^w-1)E$, and the cavity walls correspond to regions of infinite potential. In this picture the origin of each type of wavefunctions is easily explained. The key is the separability of solutions for our cavity, which allows the total energy E to be split into

$$E = E_x + \left(\frac{n\pi}{L}\right)^2, \tag{51}$$

where n is the mode index of the wave function in L direction. At constant E, E_x becomes negative for sufficiently high n, thereby confining the wave function to the lower-well region(s) of the potential, the only region(s) in the cavity allowing oscillatory waves with negative energy. Wave functions with $E_x<0$ correspond to a quantum particle classically trapped in a square-well potential. These classically trapped states are not surprising; they are "trivially localized." An example is shown in Fig. 13(a).

Not all wave functions with positive E_x are delocalized, as examples in Figs. 13(b)–13(d) show. Unlike wave functions with $E_x<0$ [see, e.g., Fig. 13(a)], these wave functions are nontrivially localized. We interpret them as resonances. Of particular interest are wave functions localized in the wax region for $E_x>0$. In the analogous quantum picture these

states correspond to a quantum particle hovering at $E_x>0$ above the potential well, confined by non-Newtonian reflections off the left and the right edge of the wax region. It is for this reason we call these wave functions *hovering states*. The left- and right-localized wave functions [see examples in Figs. 13(c) and 13(d)] have a similar origin, but they involve only a single non-Newtonian reflection. For the left- and right-localized states we compute the real and imaginary parts of their complex resonance energies. Imagine a traveling wave with energy $E_x>0$ originating in the wax region ($x<d_{\mathrm{T1}}$, $V=V_0<0$) incident on the shelf region ($x>d_{\mathrm{T1}}$, $V=0$). Define $k=\sqrt{E_x}$, $k'=\eta k$, $\eta=\sqrt{\kappa_e^w}$. Then the amplitude of the traveling wave is given by

$$\psi_{\mathrm{travel}} = e^{ik'(x-d_{\mathrm{T1}})} + re^{-ik'(x-d_{\mathrm{T1}})}, \tag{52}$$

where r is the reflection coefficient. The amplitude in the shelf region is given by

$$\psi_{\mathrm{shelf}} = A\,\sin[k(x-e)]. \tag{53}$$

Continuity of the wave function and its first derivative at $x=d_{T1}$ gives

$$A = \frac{2i\eta}{\cos(kw) - i\eta\sin(kw)}, \tag{54}$$

where $w=e-d_{\mathrm{T1}}$. The resonances occur for $\cos(kw)-i\eta\sin(kw)=0$, which yields

$$E_x^{(r)} = \frac{m\pi}{w}, \quad m=1,2,\ldots, \quad E_x^{(i)} = -\,\mathrm{arctanh}(1/\eta). \tag{55}$$

We see that the right-localized states form a sequence that can be labeled with the two quantum numbers m and n; the $(m,n)=(1,4)$ state in Fig. 13(d) is an example.

An analogous derivation leads to left-localized states; the $(m,n)=(1,5)$ state in Fig. 13(c) is an example.

Assuming infinitely high walls at $x=b_{\mathrm{T1}}$ and $x=d_{\mathrm{T1}}$ the trapped states can also be classified with an (m,n) scheme. The $(m,n)=(2,6)$ state in Fig. 13(a) is an example.

Counting the number of states with $E_x<0$ leads to the following leading-order, approximate Weyl formula for trapped states,

$$\bar{N}_{\mathrm{trapped}}(f) = \frac{2L\kappa_e^w(d_{\mathrm{T1}}-a_{\mathrm{T1}})}{c^2}\,\arcsin\left(\sqrt{\frac{\kappa_e^w-1}{\kappa_e^w}}\right)f^2. \tag{56}$$

Figure 14 shows $\bar{N}_{\mathrm{trapped}}(f)$ (smooth line) together with the exact staircase function $N_{\mathrm{trapped}}(f)$ (stepped line).

Why over most of the frequency range of Fig. 14 $N_{\mathrm{trapped}}(f)$ exceeds the analytical estimate $\bar{N}_{\mathrm{trapped}}(f)$ is easily explained. For the analytical calculations we assumed hard, infinitely high walls at $x=a_{\mathrm{T1}}$ and $x=d_{\mathrm{T1}}$, whereas the actual "softness" of these walls allows for tunneling out of the trapping region. Thus the trapped states experience a trapping region that is effectively wider than $d_{\mathrm{T1}}-a_{\mathrm{T1}}$, resulting in more trapped states than predicted by $\bar{N}_{\mathrm{trapped}}(f)$. This is analogous to the perimeter correction to the 2D Weyl formula for Neumann versus Dirichlet boundary conditions. For

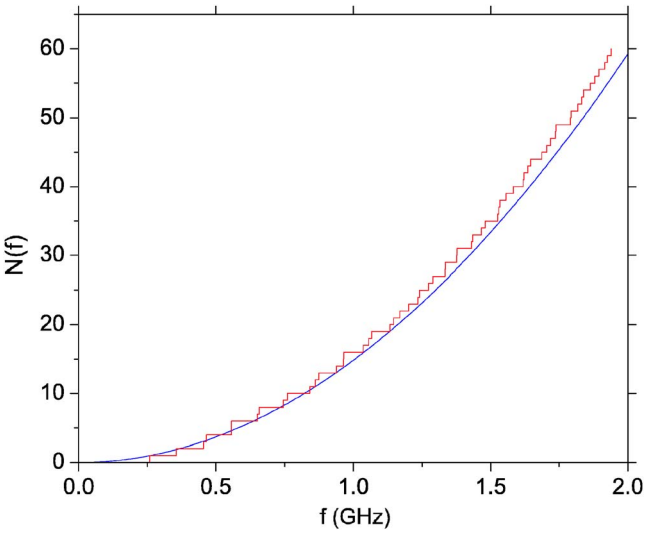

FIG. 14. (Color online) Staircase function of trapped states for the wax bars in T1 configuration. Ragged full line: Numerical result. Smooth full line: Analytical estimate of the average number of trapped states neglecting tunneling.

the latter situation the wavefunction vanishes at the boundaries (making them "hard"), and the resultant perimeter correction is negative, reducing the effective area of the resonator. For the former situation, e.g., in an air-filled 2D "room," the wave function does not vanish at the boundaries (making them softer), and the corresponding correction is positive, increasing the effective area of the resonator.

Wavefunction structures similar to those discussed above for a specific case exist generically for bars-together and even for the bars-apart configuration. However, the latter configuration offers additional possibilities for qualitatively different structures, viz., (i) states trapped (hovering) exclusively in (above) the left wax bar, (ii) states trapped (hovering) exclusively in (above) the right wax bar, (iii) states trapped (hovering) in (above) both bars, and (iv) states localized in the middle, between the bars. Of course, there are also combinations of the possibilities (i)–(iv).

We suspect that localized wave functions in our wax-loaded cavity are likely the leading cause for our beginning to miss states at $N\sim 150$ and, thus, having to cut our raw spectra from $\sim$210 states to $\sim$150 states. With a finite number of antenna-hole placements (used two at a time, see Secs. IV C, IV F, and V D), in a bars-apart configuration there may only be a single antenna hole available to probe the region of one or the other wax bar. Since our experimental protocol is based on confirming transmission peaks with different antenna placements, a state localized exclusively inside a single bar may well be rejected: it may be picked up only very weakly with just the one antenna placement, the one probing that wax bar, whereas, because of its localized nature, it goes undetected for the other placements that have no antenna in or near that wax region.

If the reason for missed states is wave-function localization, the question arises why we miss states only starting at about $N\sim 150$, while localized states occur already for $N<10$. The answer is clear. For small N the states are signifi-

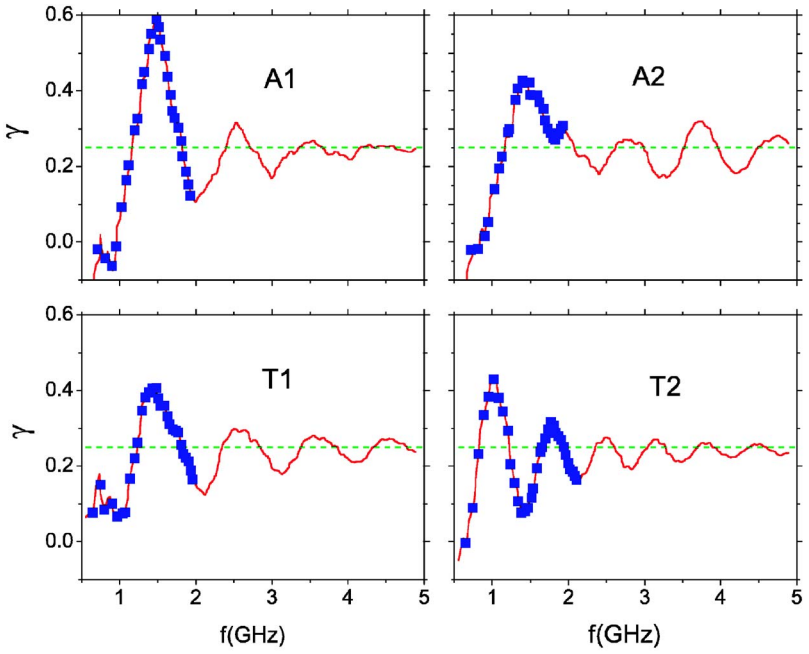

FIG. 15. (Color online) Corner correction function $\gamma(f)$ as a function of frequency for the four experimental bar placements A1, A2, T1, and T2, respectively. Full line: Numerical simulation including 1000 cavity resonances. Plot symbols: $\gamma(f)$ extracted from the experimental resonance spectra using a fitting method. The experimental results for $\gamma(f)$ (plot symbols) are identical with the numerical simulations (full lines) on the scale of the plot. For all four bar placements $\gamma(f)$ oscillates around, but is consistent with, the expected value $\gamma=1/4$ for the corner correction to the Weyl formula of a cavity with four metallic corners.

cantly "quantal," with large overlap with the classically forbidden region. As N increases, the wavelengths of the localized states decreases, and the states become inceasingly "semiclassical." This means that the component of a localized wave function outside of the localization region is very small in the semiclassical limit. In fact, tunneling vanishes completely in the classical limit of zero wavelength. Obviously this must be so since, for zero wavelength, we must recover classical physics that predicts zero occupation probability in classically forbidden regions. This is the reason why with a given antenna sensitivity there is always a cutoff N_c above which the tunneling (evanescent) component of a localized state becomes too small to be detected easily in the classically forbidden region. Apparently, in our experiments $N_c \sim 150$.

We close this section by suggesting that combining the presence of localized states with the kind of tunneling just discussed, dielectric-loaded cavities may be ideal systems for the investigation of chaotic tunneling. For previous work on chaos-assisted tunneling, see [77–84] and references therein.

VIII. CORNER CORRECTION

An additional test of the quality of our data is extraction of the corner correction (29). To our knowledge ours is the first time this is done from experimental resonance spectra. Recall that the theoretical prediction is $\bar{N}_C(f)=1/4$.

Note that a corner correction should not be present in the difference staircase obtained from our movable-bar scheme; its effect should cancel. Therefore we must extract it directly and individually from each of the four data sets A1, A2, T1, and T2. According to Eqs. (23)–(29), $\bar{N}(f)$ is of the form

$$\bar{N}(f) = \alpha f^2 + \beta f + \gamma, \tag{57}$$

where α, β, and γ are constants. Though one is tempted to fit Eq. (57) to $N(f)$ to obtain $\bar{N}_C=\gamma$, our data sets consist of fewer than 200 measured resonances, and the fluctuations in $N(f)$ are appreciable; therefore, this method does not work. However, we find that smoothing $N(f)$ by integrating it once over frequency, and then fitting a cubic polynomial to the resulting $\int_0^f N(f')df'$, does produce a γ consistent with Eq. (29). We give details next.

Let $\{f_{k;\mathrm{a}}\}$, $k=1,\ldots,n_{\mathrm{a}}^{(c)}$, $\mathrm{a}\in\{\mathrm{A1},\mathrm{A2},\mathrm{T1},\mathrm{T2}\}$, be the set of measured cavity-resonance frequencies. We define

$$M_{j;\mathrm{a}} = \int_0^{f_{j;\mathrm{a}}} N_{\mathrm{a}}(f)df = jf_{j;\mathrm{a}} - \sum_{m=1}^{j} f_{m;\mathrm{a}} \tag{58}$$

and

$$S_{k;\mathrm{a}}(\alpha,\beta,\gamma) = \sum_{j=1}^{k}\left[\frac{1}{3}\alpha f_{j;\mathrm{a}}^3 + \frac{1}{2}\beta f_{j;\mathrm{a}}^2 + \gamma f_{j;\mathrm{a}} - M_{j;\mathrm{a}}\right]^2. \tag{59}$$

Minimizing $S_{k;\mathrm{a}}$ with respect to its arguments α, β, and γ defines least-squares-fit parameters $\alpha_{\mathrm{a}}(f_k)$, $\beta_{\mathrm{a}}(f_k)$ and $\gamma_{\mathrm{a}}(f_k)$. We test the null hypothesis of $\gamma(f)$ being consistent with 1/4.

Using the above scheme we computed γ for $10<k<n_{\mathrm{a}}^{(c)}$ as a function of frequency f at the cavity resonances $f_{a,k}^{(\mathrm{expt})}$ for the four bar configurations A1, A2, T1, and T2, respectively. The results are shown in Fig. 15 as plot symbols, which extend in each case up to the respective limit of certified spectral completeness; see Sec. V. We see that in all four cases $\gamma(f)$ oscillates around the expected value $\gamma=1/4$. Configuration T2 has the greatest number of oscillations before its upper-frequency limit. In a numerical experiment there is, within reason, no limit to the number of theoretical resonances, so we computed 1000 resonance frequencies each for the "theoretical" cavity in A1, A2, T1, and T2 configuration. From them we extracted γ according to the scheme discussed above. The result is shown as the full line in the respective panels in Fig. 15. We notice in each panel

that (i) the experimental data points are close to the numerical results; (ii) both the experimental results and the numerical results oscillate around $\gamma=1/4$; (iii) as shown by the numerical results, the oscillation amplitude dies out with increasing frequency and approaches $\gamma=1/4$.

We confirmed for each of the four data sets that artificial deletion by hand of a resonance results in a "veering-off" phenomenon similar to what was discussed in Sec. V. Therefore, considering the closeness of the experimental data points to the numerical calculations in Fig. 15, as well as the absence of any "veering-off" phenomenon, result (i) provides another independent confirmation that the experimental data sets are complete up to $n_{\mathrm{a}}^{(c)}$, respectively.

Concerning item (ii), it is well known that oscillations in the staircase function $N(f)$ are due to classical periodic orbits [36]. Therefore, as discussed in more detail in Sec. X, we attribute the oscillations around $\gamma=1/4$ to the presence of controlling classical periodic orbits. It is worth noting (see Sec. X) that the shortest classical orbits, which control the slowest oscillations (with periods $\approx 0.5, \ldots, 1$ GHz in Fig. 15) are due to non-Newtonian periodic orbits [48].

The fading of the oscillations with increasing frequency, noted above in (iii), is a consequence of the fitting procedure discussed above. Fitting a smooth cubic polynomial to an integrated staircase function whose oscillations are bounded, naturally results in a more stable, convergent fit for larger fitting ranges.

It is encouraging to see that the fit approaches the expected corner correction of $\gamma=1/4$; moreover, this is of additional importance in the context of RS junctions. Theory predicts that the RS correction due to RS junctions vanishes; see Sec. II Eq. (28). Since the separation of two wax bars generates four RS junctions, we argued in Sec. III B 2 that our movable-bar experiment would be doomed to failure if the result (28) were incorrect. While we cannot rule out a frequency dependence of the RS correction due to RS junctions, which, if present, might have been absorbed in the α and β values of our fitting scheme, the corner-correction results displayed in Fig. 15 are consistent with the statement that RS junctions do not contribute a constant term to the Weyl formula. This statement is consistent with the prediction (28), i.e., $N_{\mathrm{RSJ}}(f)=0$.

In contrast to our measurements of the RS correction, our experimental results for the corner correction are not model independent: they rely on a theoretical result, viz., that the average staircase $\bar{N}(f)$ is of the form (57). Still, as far as we are aware, our extraction of the corner correction, as displayed in Fig. 15, is the first to be accomplished from experimental data.

IX. NEAREST-NEIGHBOR-SPACING STATISTICS

The spectrum of an ideal (undamped) bounded wave system such as a quantum billiard [36,60], an acoustic chamber [30–32,37], or a microwave resonator [43,44,48,60,75,85], spans a countable infinity of states [66] that become finite-width resonances when damping is included [61]. Given their great number we are often less interested in the precise values of individual resonances and more interested in characterizing the spectrum as a whole. In this case an established procedure is to characterize the spectra using statistical tools [36,60,86,87]; often one compares spectra with the results of *random matrix theory* [88,89].

A convenient and popular statistical measure for spectra is the nearest-neighbor-spacing statistics (NNSS) defined in the following way. For, e.g., a microwave resonantor, let $\{f_i\}$ be a sequence of its spectral values and $N(f)=\Sigma_{i=1}\theta(f-f_i)$ be the associated spectral staircase function, where θ is defined in (5). The following procedure creates the *unfolded spectrum*. With $\bar{s}=\langle f_{i+1}-f_i\rangle$ being the *local* average frequency spacing, we define the scaled spacings as

$$s_i = (f_{i+1} - f_i)/\bar{s}. \tag{60}$$

We then sort the set $\{s_i\}$ of scaled spacings according to their size. The NNSS of the original sequence $\{f_i\}$ is defined to be the probability density $P(s)$ of the occurrence of a spacing s in the normalized sequence $\{s_i\}$. Ideally, the sets $\{f_i\}$ and $\{s_i\}$ are (countably) infinite, but in laboratory or numerical experiments, one must work with truncated, finite sets. In the present experiment we work with finite sets from spectra known to be complete up to some cutoff; see Sec. V.

It has been conjectured [36,60,90] that the NNSS of integrable quantum systems is close to Poissonian, i.e.,

$$P(s) = P_{\mathrm{Poi}}(s) = e^{-s}. \tag{61}$$

However, it is well known that truncated, finite spectra of rectangular resonators are not well described by Poissonian statistics [91]; the Poisson case is not achieved until the semiclassical limit is reached, i.e., asymptotically high up in the spectrum [92,93]. Therefore, given demonstrated deviations lower down, i.e., in the finite, truncated spectrum [91], which is the situation that applies to our experiment, and since our cavity is close to an integrable (even separable) system, it is interesting to investigate whether our spectra do or do not have Poissonian statistics. Moreover, as discussed in Sec. VII, our cavity exhibits the phenomena of wave-function localization and tunneling. Although tunneling becomes negligible in the semiclassical limit of short wavelengths, it does play a role in our experiments, which are conducted at relatively low frequencies. Since our cavity is a time-reversal-invariant, spin-zero system, we might compare its NNSS not only with the Poissonian result but with the NNSS for time-reversal invariant, spin-zero quantum chaotic systems, the so-called Wignerian statistics,

$$P_{\mathrm{Wig}}(s) = \frac{\pi s}{2} e^{-\pi s^2/4}. \tag{62}$$

To compute the NNSS for the cavity spectra we need $\bar{N}(f)$ for use in the unfolding procedure (60). We modeled it as a cubic polynomial $\bar{N}(f)=\alpha f^3+\beta f^2+\gamma f$ and determined the parameters α, β, and γ by a least-squares fit to the experimentally measured $N(f)$.

On the basis of the $n_{\mathrm{A1}}^{(c)}=153$ resonances in the certified-complete A1 spectrum, we computed $P_{\mathrm{A1}}(s)$ as a histogram with bin width $\Delta s=0.5$ in the range $0\leqslant s\leqslant 3$, which gives

six histogram bins. As a statistical measure of the closeness of the resulting $P_{A1}(s)$ histogram to the Poissonian case (61), we computed the statistic

$$\chi^2 = \sum_{k=1}^{6} \frac{(N_k - N_k^0)^2}{N_k^0}, \tag{63}$$

where N_k is the actual number of spacings in histogram bin number k ($s_{k-1} < s < s_k$, $s_k = k\Delta s$) and $N_k^0 = (n_{A1}^{(c)} - 1)[\exp(-s_{k-1}) - \exp(-s_k)]$ is the expected number of spacings according to the Poissonian NNSS. Since we must ensure that the NNSS $P(s)$ is normalized, Eq. (63) is a χ^2 distribution with five degrees of freedom. It has expectation value $\langle\chi^2\rangle = 5$ and standard deviation $\sigma(\chi^2) = \sqrt{10} \approx 3.2$.

For the resonances of the cavity in A1 configuration we obtain $\chi^2_{A1} = 2.1$, which is comfortably within one standard deviation of the expected value $\chi^2 = 5$. For the cavity in A2 and T1 configuration we obtain $\chi^2_{A2} = 8.1$ and $\chi^2_{T1} = 4.9$, respectively, again roughly within one standard deviation. Thus, individually, the NNSS of the spectra for the A1, A2, and T1 configurations are consistent with Poissonian. The NNSS for T2 is different. We obtain $\chi^2_{T2} = 19.0$, more than three standard deviations from the expected value $\chi^2 = 5$.

Is the much larger deviation for T2 statistically significant? A look at the N_k values in the last bin of our histograms raises doubts. Although we histogrammed our data using only 6 bins, to aim at a statistically significant N_k in each bin, inspection of the sixth bin reveals $N_6 = 5, 1, 3, 4$, for A1, A2, T1, and T2, respectively. Therefore, in the sixth bin the counting errors, on the order of $\sqrt{N_6}$, are large. This means that both the favorable χ^2 results for A1, A2, and T1, and the unfavorable result for T2 may be due to low statistics.

To improve the statistics of our experiment we also calculated a *combined* NNSS $P(s) = [P_{A1}(s) + P_{A2}(s) + P_{T1}(s) + P_{T2}(s)]/4$. For this calculation we set $n_a^{(c)} = 152$, $a \in \{A1, A2, T1, T2\}$. This ensures that all four resonance sequences entering the calculation have the same length, i.e., none of the sequences is favored. Figure 16 shows the result. Visually the resulting spectral statistics is far from Wignerian (dashed line in Fig. 16) and looks close to Poissonian (solid line in Fig. 16). Calculation of χ^2 for the latter case, however, gives $\chi^2 = 11.7$, i.e., about two standard deviations from the expected $\chi^2 = 5$.

Even though we combined the statistics of four experimental spectra, the number of counts in the sixth bin is still only 13 counts, with a statistical error near four counts. Therefore we still face the question of results being skewed by low statistics. Because of the nature of the Poisson statistics (exponential drop meaning necessarily small values for large s), one always faces the problem of low counts in bin(s) at the large-s end of the distribution.

However, this is true only if we use "conventional" NNSS, which uses equispaced histogram bins. An alternative is to use a histogram with variable bin sizes set so that a nearly equal number of counts occurs in each bin. This method is called *probability binning* [94]. To effect this

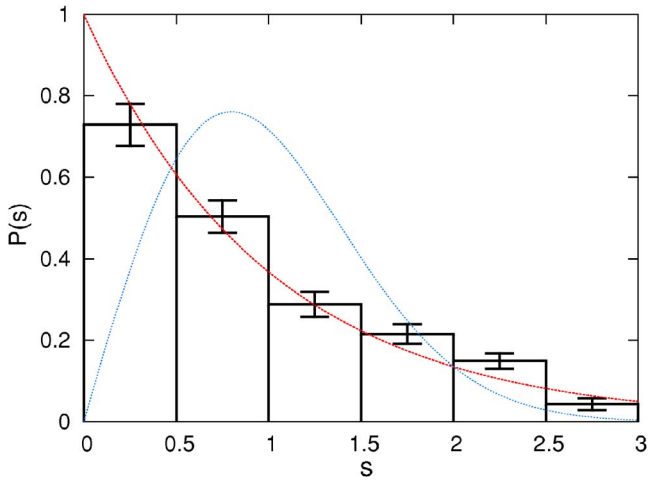

FIG. 16. (Color online) Average nearest-neighbor-spacing statistics including the first 152 resonances of the cavity in A1, A2, T1, and T2 configurations. Error bars indicate the statistical error in each bin. Smooth full line: Poissonian statistics (61). Dashed line: Wignerian statistics (62).

method for our resonance data, we again choose 6 bins but delimit them according to

$$s_k = -\ln\left(1 - \frac{k}{6}\right), \quad k = 0, \ldots, 5, \quad s_6 = \infty. \tag{64}$$

For the case of combined statistics this procedure puts an average of about 101 spacings in each histogram bin, with a statistical error of only about ten spacings, i.e., a 10% error in each bin. Since $s_6 = \infty$, probability binning also ensures that all data points are taken into account. Figure 17 shows the result. Now the columns in each bin are close to their expected value (dashed line in Fig. 17). A calculation gives $\chi^2 = 4.4$, within about one standard deviation from the value $\chi^2 = 5$ expected for Poissonian statistics. Therefore, the com-

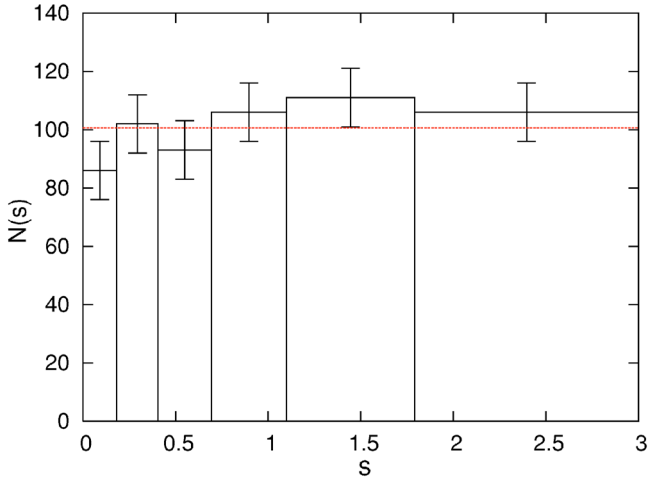

FIG. 17. (Color online) Same as Fig. 16 but using probability binning [94]. This method avoids problems with low number of counts in large-s bins.

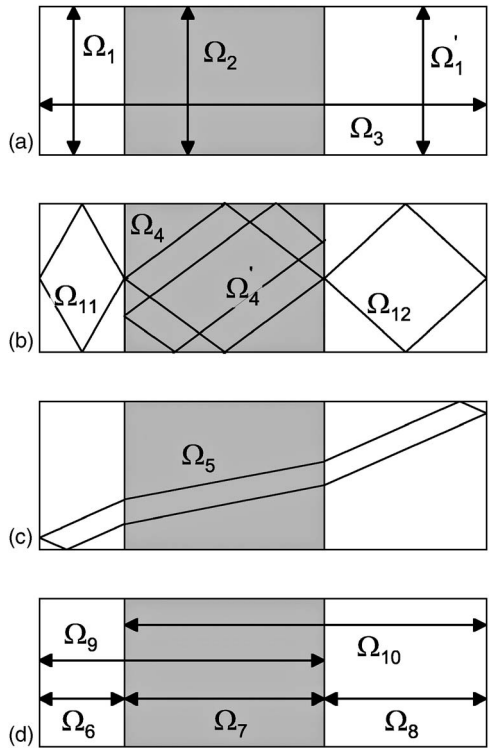

FIG. 18. Sketch of the cavity in T1 configuration (not to scale) illustrating families of Newtonian and non-Newtonian periodic orbits. (a) Newtonian bouncing-ball orbits. The families are represented by the orbits Ω_1, Ω_1' Ω_2, Ω_3 with round-trip times $t_1=6.4$ ns, $t_2=9.6$ ns, and $t_3=6.7$ ns, respectively. (b) Newtonian total-internal-reflection (diamond) orbits (Ω_4,Ω_4') and non-Newtonian diamond orbits $(\Omega_{11},\Omega_{12})$ with round-trip times $t_4=t_4'=10.3$ ns, $t_{11}=6.5$ ns, and $t_{12}=6.7$ ns, respectively. Only the most symmetric members of these families are in fact diamond shaped, as indicated by the orbit Ω_4'. (c) Family of Newtonian refraction orbits represented by Ω_5 with round-trip time $t_5=8.6$ ns. (d) Families of non-Newtonian bouncing-ball orbits represented by $\Omega_6,\ldots,\Omega_{10}$, with round-trip times $t_6=1.1$ ns, $t_7=3.7$ ns, $t_8=2.0$ ns, $t_9=4.7$ ns, $t_{10}=5.7$ ns, respectively.

bined NNSS of the four experimental resonance spectra is close to the Poissonian case.

X. PERIODIC-ORBIT SPECTROSCOPY

Periodic orbits are more than key to understanding the behavior of a chaotic classical dynamical system [95]; they open a route to a profound understanding of the corresponding quantal behavior [36]. Indeed periodic orbits turn out to control the oscillations and undulations of the RS signal in our experiment; see Figs. 10 and 11, and Sec. VI. Therefore we must discuss the periodic-orbit structure of our dielectric-loaded cavity.

Section X A begins with an exploration of the structure and round-trip times of families of short periodic orbits. Sections X B and X C present use of Fourier analysis of the experimental staircase functions to reveal the signatures of periodic orbits in the data. We use three different methods: (i) Fourier transform of the spectrum measured for a given configuration of bars; (ii) Fourier transform of the difference-staircase between bars-apart and bars-together configurations; (iii) Fourier transform of "null signals," i.e., the difference staircases between the two bars-apart cases and the two bars-together cases.

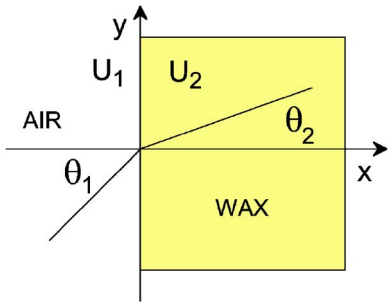

FIG. 19. (Color online) Illustration of Newtonian refraction of a classical particle passing from a region of constant potential U_1 $(x<0)$ to a region with constant potential U_2 $(x>0)$. The incident and refraction angles, measured with respect to the vertical on the interface, are θ_1 and θ_2, respectively.

In Sec. X B we show that (i) reveals both Newtonian and non-Newtonian periodic orbits. In Sec. X C we show that (ii) suppresses some and (iii) suppresses all Newtonian periodic orbits. Thus both (ii) and (iii) enhance the Fourier amplitudes corresponding to non-Newtonian orbits and provide a tool for non-Newtonian periodic-orbit spectroscopy. Because (ii) and (iii) involve differences between the staircase functions of measured spectra, we call these techniques *differential spectroscopy*.

A. Periodic orbits

We start with the energy-scaling Schrödinger equation (12). In a region with relative dielectric constant κ_e, the equivalent quantum particle has total kinetic energy

$$E_{\rm kin}=E_{\rm mech}-V(E_{\rm mech};x,y)=E_{\rm mech}+E_{\rm mech}(\kappa_e-1)=\kappa_e E_{\rm mech} \tag{65}$$

and momentum

$$p_{\rm mech}=\sqrt{2mE_{\rm kin}}=\hbar k_0\sqrt{\kappa_e}. \tag{66}$$

With the integrals taken along a given periodic orbit, the action is

$$S_{\rm mech}=\oint p_{\rm mech}ds=\hbar c k_0 t^{\rm (po)}, \tag{67}$$

where we defined the scaled round-tip time (the optical path length divided by the speed of light in vacuum)

$$t^{\rm (po)}=\frac{1}{c}\oint\sqrt{\kappa_e(x,y)}ds. \tag{68}$$

Since the Q2D cavity and its wax-bar inserts have rectangular cross sections, all periodic orbits, Newtonian and non-Newtonian, appear as families.

Consider, as an example, the cavity in T1 configuration. Figure 18 shows some of its simplest periodic orbits. Those

labeled Ω_1, Ω_2, and Ω_3 in Fig. 18(a) are representatives of families of Newtonian *bouncing-ball orbits* with round-trip times $t_{\Omega_1}=6.4$ ns, $t_{\Omega_2}=9.6$ ns and $t_{\Omega_3}=6.7$ ns, respectively.

To examine more complicated Newtonian orbits we need the classical law of refraction in two dimensions. To derive it, consider a classical particle of energy E passing from a region of constant potential U_1 $(x<0)$ into a region of constant potential U_2 $(x>0)$ as shown in Fig. 19. Without loss of generality we align the interface between the two potentials with the y axis. Since there are no forces acting parallel to this axis, the y-component of the momentum is conserved, giving

$$mv_1 \sin\theta_1 = mv_2 \sin\theta_2, \tag{69}$$

where $v_{1,2}=[2(E-U_{1,2})/m]^{1/2}$. Because the mass m cancels, we may consider velocity-rather than momentum components. Passing from an air-filled region (region 1, $U_1\approx 0$) into a wax-filled region [region 2, $U_2=-(\kappa_e^w-1)E$] gives

$$\sin\theta_2 = \frac{1}{\sqrt{\kappa_e^w}} \sin\theta_1. \tag{70}$$

Since $\kappa_e^w>1$, the refraction angle θ_2 always exists, and there is no Newtonian reflection off the air/wax interface for this case.

Passing from a wax-filled region into an air-filled region gives

$$\sin\theta_1 = \sqrt{\kappa_e^w} \sin\theta_2. \tag{71}$$

For $\theta_2<\theta_c$, where

$$\theta_c = \arcsin\left(\frac{1}{\sqrt{\kappa_e^w}}\right), \tag{72}$$

there is refraction into region 1. For $\theta_2>\theta_c$, however, the refraction angle θ_1 does not exist, and the consequence is *Newtonian total internal reflection*. The special case of $\theta_2=\theta_c$ gives *lateral ray orbits* [46,47] that skim the interface.

Labeled Ω_4 and Ω_4' in Fig. 18(b) for the cavity in T1 configuration is a family of periodic orbits that bounce entirely inside of the wax. After their most symmetric member (Ω_4), we call them *diamond orbits*.

With $\theta=\arctan[(L/(w_1+w_2)\ ]=68.9^\circ>\theta_c=42.0^\circ$, Ω_4 and Ω_4' represent a family of Newtonian total-internal-reflection orbits; their traversal time is $t_{\Omega_4}=10.3$ ns. Figure 18(c) shows a representative of a family of more complicated Newtonian orbits labeled Ω_5. Their launch angle is $\theta=57.2^\circ$, and their traversal time is $t_{\Omega_5}=8.6$ ns.

The T1 configuration also produces families of non-Newtonian orbits. Figure 18(d) shows some non-Newtonian bouncing-ball orbits with respective traversal times of $t_{\Omega_6}=1.1$ ns, $t_{\Omega_7}=3.7$ ns, $t_{\Omega_8}=2.0$ ns, $t_{\Omega_9}=4.7$ ns, and $t_{\Omega_{10}}=5.7$ ns. The non-Newtonian diamond orbits Ω_{11} and Ω_{12} shown in Fig. 18(b) are more interesting. Their respective traversal times are $t_{\Omega_{11}}=6.5$ ns and $t_{\Omega_{12}}=6.7$ ns.

B. Fourier transform

In this section we show how Fourier transforms of the experimentally measured staircase functions reveal the periodic orbits discussed in the previous subsection.

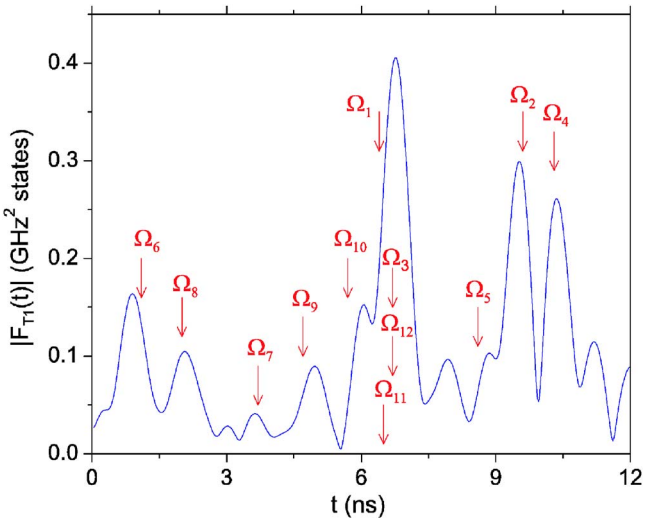

FIG. 20. (Color online) Absolute value of the Fourier transform of the first 158 resonances of the cavity in T1 configuration. The peaks in the Fourier transform can be assigned to the periodic orbits sketched in Fig. 18. The labeled arrows point to the transit times t_j corresponding to the associated periodic orbits Ω_j (see Fig. 18).

According to Gutzwiller [36] any quantum mechanical staircase function can be written as a sum of the smooth (Weyl) part $\bar{N}$ and the fluctuating part $\tilde{N}$. The latter can be expanded according to

$$\tilde{N} = \sum_{\text{po}} A^{(\text{po})} \exp(iS_{\text{mech}}^{(\text{po})}/\hbar) = \sum_{\text{po}} A^{(\text{po})} \exp(i\Phi^{(\text{po})}), \tag{73}$$

where the sum is over all classical periodic orbits of the system. For energy-scaling systems, which includes our experiment (see Sec. II), the amplitudes $A^{(\text{po})}$ are constants, independent of the energy. With Eq. (67) and $k_0=2\pi/\lambda=2\pi f/c$, we may write the phases in (73) as

$$\Phi^{(\text{po})} = 2\pi f t^{(\text{po})}. \tag{74}$$

Thus, expressed in terms of frequency, we obtain

$$N(f) = \bar{N}(f) + \tilde{N}(f) = \bar{N}(f) + \sum_{\text{po}} A^{(\text{po})} \exp(2\pi i t^{(\text{po})} f). \tag{75}$$

According to Eq. (75) $\tilde{N}(f)$ is a sum of purely oscillatory terms, which causes the Fourier transform of $\tilde{N}(f)$ to be sharply peaked at round-trip times of the classical periodic orbits. The Fourier transform of the fluctuating part of the T1 staircase is given by

$$F_{\text{T1}}(t) = \int_0^{f_{\max}} [N_{\text{T1}}(f) - \bar{N}_{\text{T1}}(f)] e^{-2\pi i t f} df, \tag{76}$$

where $\bar{N}_{\text{T1}}(f)$ is a smooth (least-squares) fit to $N_{\text{T1}}(f)$.

Figure 20 shows $|F_{\text{T1}}(t)|$. All the periodic orbits discussed in Sec. X A contribute to the peaks, but some contain unresolved contributions from orbits with nearly the same traversal times. We also notice that some arrows in Fig. 20 do

not point precisely to the maxima of corresponding peaks. We attribute this phenomenon to the finite number $n_{\mathrm{T1}}^{(c)}=158$ of resonances available in our T1 data set and the corresponding limitation $f_{\max}=f_{\mathrm{T1},158}^{(\mathrm{expt})}<2$ GHz in the frequency range of the Fourier intergral (76). While we do not have a detailed theory of peak shifts versus $f_{\max}$, we observe a similar phenomenon in numerical simulations of $|F_{\mathrm{T1}}(t)|$.

Some peaks have smaller amplitudes than others. Why, for example, Ω_7 is so small is easily understood. The (intensity) probability for reflection from the wax bar, from [46], is

$$R=\left(\frac{\sqrt{\kappa_e^w}-1}{\sqrt{\kappa_e^w}+1}\right)^2\approx 0.04. \tag{77}$$

Though all other non-Newtonian orbits in Fig. 18(d) involve only a single reflection off an air/wax (wax/air) interface, the orbit Ω_7 bounces entirely within the wax, making two reflections off the wax/air interface. Its total reflection probability of $R^2\approx 0.0016$ produces a peak that is too small to rise significantly above the background; it may just be visible in Fig. 20.

The periodic-orbit structure of the cavity in A1 configuration is similar to that of T1, but there are two important new features.

(i) The gap between the two wax bars in A1 allows for additional families of non-Newtonian periodic orbits that are not present in T1.

(ii) The single family of internal-reflection orbits Ω_4 for T1 [see Fig. 18(b)] splits for A1 into two families, Ω_{13} and Ω_{14} with respective traversal times $t_{\Omega_{13}}=9.7$ ns and $t_{\Omega_{14}}=9.8$ ns. Note that this will be important in the discussion, below, of the fine details of Figs. 10 and 11.

C. Differential spectroscopy

The experimental signal discussed in Sec. VI is not the staircase function $N(f)$ but the integrated difference (35) of two staircases

$$I_{a_1a_2}(f)=\int_0^f [N_{a_1}(f')-N_{a_2}(f')]df', \tag{78}$$

where $a_1,a_2\in\{A1,A2,T1,T2\}$ denote bar placements. Since an integration of the staircase function over frequency does not change the structure of (75), we obtain

$$I_{a_1,a_2}(f)=\bar{I}_{a_1,a_2}(f)+\sum_{\mathrm{po}} B_{a_1,a_2}^{(\mathrm{po})}\exp[2\pi i t_{a_1,a_2}^{(\mathrm{po})}f], \tag{79}$$

where $B_{a_1,a_2}^{(\mathrm{po})}=A_{a_1,a_2}^{(\mathrm{po})}/(2\pi i t_{a_1,a_2}^{(\mathrm{po})})$ are constants, and the sum is over all periodic orbits of the cavity with bar placements a_1 and a_2. With

$$\tilde{I}_{a_1,a_2}(f)=I_{a_1,a_2}(f)-\bar{I}_{a_1,a_2}(f) \tag{80}$$

denoting the fluctuating part of $I_{a_1,a_2}(f)$, its Fourier transform is

$$F_{a_1,a_2}(t)=\int_0^{f_{\max}}\tilde{I}_{a_1,a_2}(f)\exp(-2\pi i t f)df. \tag{81}$$

Using Eq. (79) we obtain

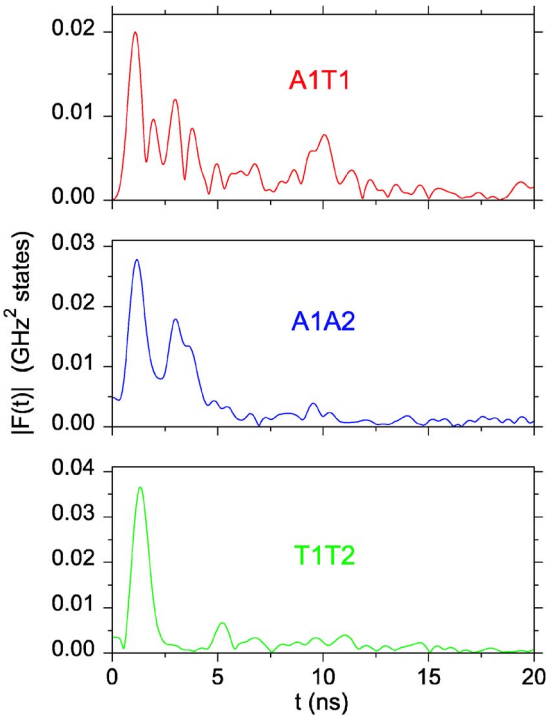

FIG. 21. (Color online) Absolute values $|F_{\mathrm{A1T1}}|$ top panel, $|F_{\mathrm{A1A2}}|$ middle panel, and $|F_{\mathrm{T1T2}}|$ bottom panel, of the Fourier transforms of the integrated differences $\tilde{I}_{\mathrm{A1T1}}$, $\tilde{I}_{\mathrm{A1A2}}$, and $\tilde{I}_{\mathrm{T1T2}}$, respectively.

$$F_{a_1,a_2}(t)=\sum_{\mathrm{po}} B_{a_1,a_2}^{(\mathrm{po})}\exp[-i\pi f_{\max}(t-t_{a_1,a_2}^{(\mathrm{po})})]\times\frac{\sin[\pi f_{\max}(t-t_{a_1,a_2}^{(\mathrm{po})})]}{\pi[t-t_{a_1,a_2}^{(\mathrm{po})}]}, \tag{82}$$

which, for large $f_{\max}$, is sharply peaked at $t_{a_1,a_2}^{(\mathrm{po})}$. In this way we extract periodic-orbit information from the experimentally measured $I_{a_1a_2}(f)$.

The top panel in Fig. 21 shows the absolute value of the Fourier transform $F_{\mathrm{A1T1}}(t)$ of $\tilde{I}_{\mathrm{A1T1}}(f)$ obtained with use of $\bar{I}_{\mathrm{A1T1}}(f)=0.0575[f\ (\mathrm{GHz})]^2$ GHz states. Conspicuous in $|F_{\mathrm{A1T1}}(t)|$ is a cluster of peaks at $t=1,2,3,4$ ns and a broad peak at $t\approx 10$ ns. Families of Newtonian internal-reflection orbits, e.g., Ω_4 of T1 and analogous orbits of A1, produce the broad peak at 10 ns and are reponsible for the oscillations with ~0.1 GHz period in the A1T1 panel of Fig. 10. On the other hand, the cluster of moderately strong peaks at $t=1,2,3,4$ ns, all corresponding to short non-Newtonian orbits of A1 and T1, is responsible for the undulations of $I_{\mathrm{A1T1}}(f)$ in Fig. 10.

The middle panel in Fig. 21 shows the absolute value of the Fourier transform $F_{\mathrm{A1A2}}(t)$ of $\tilde{I}_{\mathrm{A1A2}}(f)$, obtained with use of $\bar{I}_{\mathrm{A1A2}}(f)=0$, which is consistent with the RS correction vanishing for this case. Note that compared to $|F_{\mathrm{A1T1}}(t)|$, the peak at $t=10$ ns is now suppressed because the Newtonian internal-reflection orbits Ω_{13} and Ω_{14} cancel each other in A1 and A2, respectively. This happens because the sole differ-

ence between A1 and A2 is the *placements* of the bars; their *widths* remain the same.

The absence of the $t=10$ ns peak in the Fourier transform of $\tilde{I}_{\mathrm{A1A2}}(f)$ explains the near-absence of oscillations in the A1A2 panel of Fig. 10; however, the undulations in that panel are not suppressed. They are caused by the prominent peaks at $t=1,3,4$ ns in $|F_{\mathrm{A1A2}}(t)|$, which are due to short, non-Newtonian orbits in the A1 and A2 configurations, respectively. Because the contributions of all Newtonian orbits cancel when taking the A1A2 difference, the cluster of peaks corresponding to these non-Newtonian orbits is the most prominent feature in $|F_{\mathrm{A1A2}}(t)|$. The reason for this is that, independent of their placement, the wax bars act like parallel-plate beam splitters that do not change the lengths of Newtonian orbits. With the resultant cancellation of the contributions of Newtonian orbits, the Fourier spectrum is dominated by the non-Newtonian orbits.

Thus our method of calculating the Fourier transform of the *difference* (integrated difference) of staircases greatly *enhances* the signatures of non-Newtonian orbits in the Fourier transform and provides the route to their study by differential spectroscopy.

The bottom panel in Fig. 21 shows the absolute value of the Fourier transform $F_{\mathrm{T1T2}}(t)$ of $\tilde{I}_{\mathrm{T1T2}}(f)$ obtained, as for the A1A2 case, with use of $\bar{I}_{\mathrm{T1T2}}=0$, consistent with a vanishing RS signal. As for $|F_{\mathrm{A1A2}}(t)|$, and for the same reasons, the peak at $t=10$ ns is absent; this leads to the absence of oscillations in the T2T1 panel of Fig. 10. The large peak at 1 ns, due to non-Newtonian orbits in the T1 and T2 configurations, respectively, explains the presence of undulations in the T2T1-panel of Fig. 10.

There is a marked difference between I_{A1T1} and I_{A1T2} in Fig. 10. While I_{A1T1} appears relatively smooth and close to the theoretical expectation $\bar{I}^{(\mathrm{ana})}(f)$, I_{A1T2} shows a pronounced slow undulation around $\bar{I}^{(\mathrm{ana})}(f)$ with a period of about 1 GHz. The reason is the different bar placements for the two cases. Compared to the placements for A1T1, the placements for A1T2 produce many more short, non-Newtonian periodic orbits having traversal times near 1 ns; these orbits explain the aforementioned undulation in the A1T2 panel in Fig. 10. The same reason explains the different appearance of the A2T1 panel compared with the A2T2 panel in Fig. 10. Since all four bar placements, A1T1, A1T2, A2T1, A2T2 enter with equal weights in the average integrated difference displayed in Fig. 11, the two "smoother" contributions from A1T1 and A2T1 are insufficient to counterbalance the strong undulations present for the A1T2 and A2T2 configurations. Thus the undulations in the average integrated difference shown in Fig. 11 are due to insufficient averaging and an accidental clustering of short non-Newtonian orbits of about the same round-trip times in two of the four bar placement combinations we happened to choose for our experiments.

XI. DISCUSSION

One of the most fundamental counting functions is the one that counts prime numbers. A smooth approximation to its staircase function (a Weyl formula for prime numbers) lies at the heart of number theory and connects to much of mathematics. The prime number theorem that Hadamard and de la Vallée-Poussin proved in 1896 establishes that the average density of primes in the neighborhood of large x is $\sim 1/\ln x$ to leading order. For accessible reviews see [96–98].

Rooted in mathematics, counting functions soon found important applications in physics. Nine decades after Weyl's seminal work [10–12] smooth approximations to counting functions (Weyl formulas) remain a focus of current research. Our contribution here comes from the experimental measurements of the RS correction in a dielectric-loaded Q2D cavity.

Experimental Q2D cavity physics started with the acoustical research of Bolt in the late 1930s [37]. Five decades later Q2D microwave resonators were introduced in quick succession by Stöckmann and Stein [44] and Sridhar [85] as model systems for experiments in quantum chaos [36]. Since then Q2D cavity physics has been developed by many researchers into a powerful tool for the study of spectra of classically chaotic systems [43,44,48,49,51–59,75] and references therein.

Loading such cavities with dielectric inserts has provided a new direction for Q2D-cavity physics: they are ideal for investigation of RS phenomena. The first such experiment [48] discovered non-Newtonian orbits with a Bunimovich-stadium-shaped Q2D microwave cavity loaded with a Teflon bar. Successive experiments investigated RS phenomena [43,49,52,58] or related diffractive phenomena [56,57] with dielectric-or metal-loaded cavities. Another experiment [99] investigated a Sinai billiard loaded with a quarter-circle Teflon insert that caused RS, though the focus of this work was not on extraction of the RS correction to the Weyl formula from experimental spectra but on the determination of RS periodic orbits and visualization of wave functions. Unfolding of the experimental spectrum [36,60] in [99] required the mean staircase function that included a RS correction put in from theory [38,46,67].

While previous experiments with Q2D cavities addressed some aspects of RS, not until our announcement in [42], brief publication in [43], and detailed presentation in this paper has an experiment demonstrated the existence of the RS correction to the Weyl formula. As Secs. II and VI discuss, the smallness of the RS effect and its extraordinary sensitivity to variations in the cavity geometry were problems that had to be surpassed.

One example is lid buckling; see Sec. VI D. Though resonance frequencies of an ideal cavity are independent of the cavity's height (in the z dimension) in the Q2D regime below $f_{\mathrm{3D}}^{\mathrm{min}}$ [see Eq. (7)], they are not if the cavity height is nonuniform. We were surprised to find just how sensitive our experiment is to lid buckling; local height variations at the sub-percent level significantly affect the RS results. It happens because lid buckling produces electric fields with x and y components. In our case these components are certainly weak compared to the mean amplitude of the z component, but formally their existence makes the cavity geometry 3D and breaks the equivalence of the Maxwell equations with the 2D Helmholtz (Schrödinger) equation.

Had we anticipated the seriousness of this effect, we would have used a sturdier (aluminum) plate rather than circuit board for the top lid of the cavity. Nevertheless, once we understood this effect we used Mylar spacers and crossbars (see Sec. VI) to keep it under control and allow extraction of the RS effect from spectra obtained with the circuit-board top lid.

This paper does more than strenghten our first brief account [43] of measuring the RS correction to the Weyl formula. The rest of this section discusses important additional results: differential spectroscopy (Sec. XI A), wave-function localization (Sec. XI B), and a measurement of the corner correction to the Weyl formula (Sec. XI C).

A. Differential spectroscopy

Non-Newtonian RS orbits are central to the theory of RS systems. Though their existence was predicted over a decade ago [39,40,45], only the simplest such orbits (non-Newtonian bouncing-ball orbits) have yet been visualized from Fourier transforms of experimental spectra [48,99]. This paper introduces study of more complicated non-Newtonian orbits, such as Ω_{11} and Ω_{12} [see Fig. 18(b)], though Fig. 20 shows they are not resolved. As is the case in Fig. 20, this is often caused by the signature of non-Newtonian orbits in Fourier transforms being "drowned out" by strong, broad peaks produced by Newtonian orbits.

Differential spectroscopy subtracts the effect of Newtonian orbits and furnishes the first route for experimental detection of the signatures of more complicated non-Newtonian orbits. Differential spectroscopy may also allow observation of lateral-ray orbits [39,40,46,47].

B. Wave-function localization

A dielectric insert with sharp edges in a Q2D microwave cavity does more than create non-Newtonian orbits and a correction to the Weyl formula. It also produces localized wave functions. Section VII presented several examples that fall, roughly, into a "trivial" or a "nontrivial" class. Wave functions with $E_x<0$ concentrated inside the wax-bar region [see Fig. 13(a)] are trivially localized and unsurprising. In the analogous quantum picture (see Sec. II) these wave functions correspond to a quantum particle confined inside a square-well potential. The three other types of states shown in Figs. 13(b)–13(d), however, are more interesting because the mechanism that localizes them has nontrivial origin. These states require non-Newtonian reflections off one air-wax interface [left- and right-localized states, see Figs. 13(c) and 13(d)] or off two air-wax interfaces [hovering states, see Fig. 13(b)].

The ubiquity of hovering states surprised us. Let us define the localization fraction as the overlap probability of a cavity state with the region of the wax bars. For our cavity the fraction of total area occupied by the wax bars is $p_A = 37/82.69 \simeq 0.447$. We call a state localized in the region of the wax bars if its localization fraction exceeds p_A. Among the first 158 states in the complete T1 spectrum, we find 72 states with a localization fraction larger than p_A. Since the $E_x<0$ trapped states number 62, there must be ten hovering states among the first 158 T1 resonances. They are not uncommon.

C. Corner correction

An interesting historical question arises in connection with perimeter and corner corrections to the Weyl formula. Who first correctly presented the corner correction for a resonator? Balian and Bloch state in [13], but they give no supporting reference, that Weyl conjectured the correct form of the perimeter correction. As far as we have been able to ascertain, Maa [32] published the first correct perimeter and corner corrections, in his case for the rectangular parallelepiped acoustical resonator (Neumann boundary conditions). We are unaware of an experimental measurement of the corner correction and, therefore, believe that the results we reported in Sec. VIII are the first measurements of a corner correction.

The corner correction signals (see Fig. 15) show strong oscillations around the expected value $\gamma=1/4$. We are confident that these oscillations are controlled by the shortest periodic orbits of the corresponding classical billiard. Taking the T1 case as an example (see T1 panel in Fig. 15), the dominant oscillation in $\gamma(f)$ has a frequency of about 1 GHz. This corresponds to a periodic-orbit round-trip time of about 1 ns, which is close to the round-trip time of the non-Newtonian orbit Ω_6 in Fig. 18.

Using periodic orbits as input may allow to predict the $\gamma(f)$ curve and then to fit the experimental measurements to it. This may provide a more accurate measurement of the corner correction since the fitting procedure would account for the oscillations in $\gamma(f)$. However, since the extraction of $\gamma(f)$ itself requires a fit to the integrated staircase function, we suspect that the required analytical calculations will likely be involved and have not yet attempted them.

Now we switch attention to the T2 case (see T2 panel of Fig. 15), for which we measured the longest stretch of complete resonances. We are fortunate that the dominant oscillation is fast ($\approx$0.7 GHz) for the T2 case, which allows us to follow the experimental $\gamma(f)$ signal over more than one complete oscillation. Over 1.5 periods (three half periods) of the $\gamma(f)$ signal, from $f=1.013$ GHz [where $\gamma(f)$ reaches its first maximum] to $f=2.120$ GHz [where $\gamma(f)$ reaches its second minimum], the average of $\gamma(f)$ is $\bar{\gamma}=0.22$, which is in good agreement with the theoretical value $\gamma=1/4$.

XII. OUTLOOK

This section lists several topics that should provide stimulus for further experimental and theoretical study of Weyl formulas for RS systems. They show that even a decade after the first RS correction to the Weyl formula was suggested [38], such investigations are far from exhausted.

A. Fractal RS boundaries

Our experiment demonstrates the existence of a RS correction and provides quantitative results close to theoretical expectations. However, the RS correction (26) applies to

smooth interfaces, i.e., interfaces whose local radius of curvature is much larger than the wavelength. Because previous work [Ref. [8], Sec. VI.1.(a)] informs us that the infinite-curvature limit of the smooth-curvature correction does not give the sharp-corner correction, we must exercise care to obtain the frequency dependence of the RS correction for fractal boundaries.

An elementary reason for why (26) has to be wrong for fractal RS boundaries is the following: (26) predicts that $\bar{N}_{\mathrm{RS}}(f)$ is proportional to the length of the RS boundary. Because the length of the perimeter of a fractal is well known to be infinite, proceeding blindly would give an infinite RS correction, clearly an absurd result. To conjecture the correct form of the RS correction for fractal boundaries, we make use of the analogy of the RS boundary to an ordinary Dirichlet or Neumann boundary. In this case, and in the high-frequency limit, Berry conjectured that the perimeter correction should be proportional to f^D [100,101]. Therefore, we conjecture

$$\bar{N}_{\mathrm{RS}}(f) = \mathrm{const} \times f^D \tag{83}$$

for fractal RS boundaries of fractal dimension D.

Though one cannot realize a true fractal experimentally, all the way to and beyond atomic dimensions, one may approximate it with the first few "fractal generations" [102,103]. For such a "finite resolution fractal" experimental measurement of the RS correction for a fractal boundary may be feasible with the following techniques. (i) The "tesselation trick" used in this paper, which eliminates RS boundaries by forming one solid shape from two or more partial shapes, remains applicable. We may imagine machining both a finite resolution fractal and its "negative" and performing the analog of the movable-bar technique to measure the fractal RS correction. The two (approximate) fractal surfaces cannot be slid into each other, but they can be fitted snugly into each other. (ii) A key reason for using the movable bar technique in the present work is to be able to separate the RS correction from the perimeter correction; for smooth RS boundaries they have the same frequency dependence $\sim f^1$. For fractals the perimeter correction is still $\sim f^1$, but the RS correction due to the fractal boundary is $\sim f^D$. Therefore, the two corrections should *separate*, suggesting that the movable-bar trick, at least in principle, will no longer be necessary.

Nevertheless, if model-independent results are desirable (no assumptions about the Weyl corrections for areas, perimeters, and corners) method (i) with the "tesselation trick" is preferable.

B. RS in 3D

RS with microwaves in 3D is a research direction that, so far, has received no attention at all. The 3D RS systems that have been investigated in some detail, with RS Weyl corrections computed analytically [67], are quantum systems that require only a scalar 3D theory. For microwave experiments a vector theory of RS in 3D based on the full set of Maxwell equations will be required [61]. We may imagine that qualitatively new RS phenomena will emerge in these situations.

C. RS with left-handed materials

After pioneering theoretical work nearly four decades ago on so-called left-handed materials [104], a new class of refracting metamaterials that can have a negative index of refraction was discovered recently; see [105] for a review and references. Though these materials provide a fascinating new test arena for RS phenomena and present an immediate challenge for the development of new RS theory, we believe that RS experiments with them will be difficult because their refracting properties are strongly frequency dependent. Nevertheless, with large enough cavities it may be possible to overcome this problem. Given any frequency interval $\Delta f := [f_{\min}, f_{\max}]$ over which the refractive index of a given metamaterial is reasonably constant, a spectrum having any given number N of resonance frequencies over the interval Δf will be provided by a sufficiently large cavity partially filled by the metamaterial.

D. RS curvature correction

A recent paper [106] predicts that the RS curvature correction vanishes for a class of annular ray-splitting billiards. This surprising result calls for an experimental confirmation. The measurement of RS curvature corrections is difficult because it is unclear whether there exists for this type of measurement an appropriate tesselation trick. We leave this problem as a challenge for future experimental and computational work.

XIII. SUMMARY AND CONCLUSIONS

Using a microwave cavity in the shape of a rectangular parallelepiped and partially filled with movable dielectric (wax) bars, we present experimental evidence for the validity of the RS correction predicted by Prange *et al.* [38] for wave systems containing an abrupt change in the properties of the wave propagation medium. For each of four different bar placements, we measure complete microwave spectra consisting of approximately 150 resonances each. We compare the experimentally determined integrated difference $I^{(\mathrm{expt})}(f)$ between apart and together placements of the wax bars with the analytical prediction and find good agreement. Our experimental method, based on movable wax bars, does not require any fitting of experimentally determined staircase functions and provides, thereby, a model-independent procedure for measuring the RS correction. Because of the known equivalence between flat microwave cavities and two-dimensional quantum billiards [38,44,67] our results are directly relevant to quantum systems with ray splitting. We exploit this equivalence to explain fine oscillations and coarse undulations in $I^{(\mathrm{expt})}(f)$ on the basis of Newtonian and non-Newtonian periodic orbits in the corresponding energy-scaling quantum billiards. Using the statistical method of probability binning [94] we show that the nearest-neighbor-spacing statistics of our experimental spectra are consistent with Poissonian statistics.

We discover localized wave functions that we conjecture will appear universally in all dielectric-loaded cavities: (i) states that are classically trapped inside of the dielectric re-

gions, (ii) hovering states that are confined to dielectric regions by non-Newtonian reflections, (iii) states that are localized in regions between the cavity walls and the dielectric (in our case, left- and right-localized states). We explain the left- and right-localized states as a simple resonance phenomenon and compute their complex energies.

Our experimental microwave spectra have sufficient extent and accuracy to test the corner correction N_C to the Weyl formula. Our experimental results are consistent with the theoretical prediction $N_C=1/4$ for four 90° metallic corners. To our knowledge this is the first time that the corner correction has been extracted from an experimental spectrum.

Finally, we show how the movable-bar setup enables suppression of the contributions of Newtonian periodic orbits to the Fourier transform of $I^{(\mathrm{expt})}(f)$, thereby enhancing the contributions of non-Newtonian orbits. This provides a new experimental tool for periodic-orbit spectroscopy that will facilitate the study of non-Newtonian classical physics.

ACKNOWLEDGMENTS

The authors gratefully acknowledge financial support by NSF Grants No. PHY-9984075 (to Wesleyan) and No. PHY-0099398 (to Stony Brook).

[1] W. W. R. Ball, *A Short Account of the History of Mathematics*, 4th ed. (Macmillan, London, 1908).
[2] B. Greene, *The Elegant Universe* (Vintage Books, New York, 1999).
[3] A. Pais, *Subtle is the Lord: The Science and the Life of Albert Einstein* (Oxford University Press, Oxford, 1982).
[4] http://www.claymath.org/millenium/Yang-Mills_Theory/
[5] H. J. Bernstein and A. V. Phillips, Sci. Am. **245**, 122 (1981).
[6] M. Kac, Am. Math. Monthly **73**, 1 (1966). This is the celebrated article "Can One Hear the Shape of a Drum?".
[7] Four score and four years earlier another author anticipated the title of Kac's article, Ref. [6]. See W. McGucken, *Nineteenth-Century Spectroscopy* (Johns Hopkins Press, Baltimore, 1969), p. 126, which includes the following in a quote from A. Schuster, Rep. Br. Assoc. **50**, 120 (1882): "We know a great deal more about the forces which produce the vibrations of sound than about those which produce the vibrations of light. To find out the different tunes sent out by a vibrating system is a problem which may or may not be solvable in certain special cases, but it would baffle the most skilful mathematician to solve the inverse problem and to find out the shape of a bell by means of the sounds which it is capable of sending out. And this is the problem which ultimately spectroscopy hopes to solve in the case of light. In the meantime we must welcome with delight even the smallest step in the desired direction."
[8] H. P. Baltes and E. R. Hilf, *Spectra of Finite Systems: A Review of Weyl's Problem: The eigenvalue distribution of the wave equation for finite domains and its applications to the physics of small systems* (Bibliographisches Institut Wissenschaftsverlag, Mannheim, 1976).
[9] H. A. Lorentz, Phys. Z. **11**, 1234 (1910).
[10] H. Weyl, Gött. Nachr. **1911** (Feb.), 110.
[11] H. Weyl, Math. Ann. **71**, 441 (1912).
[12] H. Weyl, J. Reine Angew. Math. **141**, 1 (1912).
[13] R. Balian and C. Bloch, Ann. Phys. (N.Y.) **60**, 401 (1970), **84**, 559(E) (1974).
[14] S. Deus, P. M. Koch, and L. Sirko, Phys. Rev. E **52**, 1146 (1995).
[15] J. H. Jeans, Philos. Mag. **10**, 91 (1905).
[16] H. A. Lorentz, in *Atti del IV Congresso Internazionale dei Matematici, Roma, 1908*, edited by G. Castelnuovo (Accademica dei Lincei, Roma, 1909), Vol. I, pp. 145–165.
[17] A. Sommerfeld, Phys. Z. **11**, 1061 (1910).
[18] J. Reudler, Ph.D. thesis, Rijks Universiteit te Leiden (Instituut Lorentz), 1912 (unpublished).
[19] H. Weyl, J. Reine Angew. Math. **141**, 163 (1912).
[20] H. Weyl, J. Reine Angew. Math. **143**, 177 (1913).
[21] H. Weyl, Rend. Circ. Mat. Palermo **39**, 1 (1915).
[22] R. Courant and D. Hilbert, *Methoden der Mathematischen Physik* (Julius Springer, Berlin, 1924).
[23] M. J. O. Strutt, Philos. Mag. **8**, 236 (1928).
[24] M. J. O. Strutt, Math. Ann. **102**, 671 (1930).
[25] F. V. Hunt, L. L. Beranek, and D.-Y. Maa, J. Acoust. Soc. Am. **11**, 80 (1939).
[26] G. M. Roe, J. Acoust. Soc. Am. **13**, 1 (1941).
[27] W. C. Sabine, *Collected Papers on Acoustics* (Harvard University Press, Cambridge, 1922; reprinted Dover, Mineola, NY, 1964).
[28] P. M. Morse, *Vibration and Sound*, 1st ed. (McGraw-Hill, New York, 1936).
[29] O. Cramer, J. Acoust. Soc. Am. **93**, 2510 (1993).
[30] R. H. Bolt, J. Acoust. Soc. Am. **10**, 228 (1939).
[31] R. H. Bolt, J. Acoust. Soc. Am. **11**, 184 (1939).
[32] D.-Y. Maa, J. Acoust. Soc. Am. **10**, 235 (1939).
[33] P. M. Morse, *Vibration and Sound*, 2nd ed. (McGraw-Hill, New York, 1948).
[34] P. M. Morse and K. U. Ingard, *Theoretical Acoustics* (McGraw-Hill, New York, 1968).
[35] P. M. Morse and R. H. Bolt, Rev. Mod. Phys. **16**, 69 (1944).
[36] M. C. Gutzwiller, *Chaos in Classical and Quantum Mechanics* (Springer, New York, 1990).
[37] R. H. Bolt, J. Acoust. Soc. Am. **11**, 74 (1939).
[38] R. E. Prange, E. Ott, T. M. Antonsen, Jr., B. Georgeot, and R. Blümel, Phys. Rev. E **53**, 207 (1996).
[39] R. Blümel, T. M. Antonsen, Jr., B. Georgeot, E. Ott, and R. E. Prange, Phys. Rev. Lett. **76**, 2476 (1996).
[40] R. Blümel, T. M. Antonsen, Jr., B. Georgeot, E. Ott, and R. E. Prange, Phys. Rev. E **53**, 3284 (1996).
[41] C. Vaa, Ph.D. thesis, State University of New York at Stony Brook (Department of Physics and Astronomy) 2003 (unpublished).
[42] C. Vaa, P. M. Koch, and R. Blümel, Bull. Am. Phys. Soc. **47**, 107 (2002).
[43] C. Vaa, P. M. Koch, and R. Blümel, Phys. Rev. Lett. **90**, 194102 (2003).
[44] H.-J. Stöckmann and J. Stein, Phys. Rev. Lett. **64**, 2215

(1990).
[45] L. Couchman, E. Ott, and T. M. Antonsen, Jr., Phys. Rev. A **46**, 6193 (1992).
[46] A. Kohler and R. Blümel, Phys. Lett. A **247**, 87 (1998).
[47] L. M. Brekhovskikh, *Waves in Layered Media* (Academic Press, New York, 1960).
[48] L. Sirko, P. M. Koch, and R. Blümel, Phys. Rev. Lett. **78**, 2940 (1997).
[49] Sz. Bauch, A. Błędowski, L. Sirko, P. M. Koch, and R. Blümel, Phys. Rev. E **57**, 304 (1998).
[50] R. Blümel, Acta Phys. Pol. A **93**, 7 (1998).
[51] R. Blümel, P. M. Koch, and L. Sirko, Found. Phys. **31**, 269 (2001).
[52] N. Savytskyy, A. Kohler, Sz. Bauch, R. Blümel, and L. Sirko, Phys. Rev. E **64**, 036211 (2001).
[53] W. T. Lu, S. Sridhar, and M. Zworski, Phys. Rev. Lett. **91**, 154101 (2003).
[54] C. Dembowski, H.-D. Gräf, A. Heine, T. Hesse, H. Rehfeld, and A. Richter, Phys. Rev. Lett. **86**, 3284 (2001).
[55] S. Sridhar, D. O. Hogenboom, and B. A. Willemsen, J. Stat. Phys. **68**, 239 (1992).
[56] J. S. Hersch, M. R. Haggerty, and E. J. Heller, Phys. Rev. Lett. **83**, 5342 (1999).
[57] J. S. Hersch, M. R. Haggerty, and E. J. Heller, Phys. Rev. E **62**, 4873 (2000).
[58] Y. Hlushchuk, A. Kohler, Sz. Bauch, L. Sirko, R. Blümel, M. Barth, and H.-J. Stöckmann, Phys. Rev. E **61**, 366 (2000).
[59] L. Sirko, Sz. Bauch, Y. Hlushchuk, P. M. Koch, R. Blümel, M. Barth, U. Kuhl, and H.-J. Stöckmann, Phys. Lett. A **266**, 331 (2000).
[60] H.-J. Stöckmann, *Quantum Chaos* (Cambridge University Press, New York, 1999).
[61] J. D. Jackson, *Classical Electrodynamics*, 2nd ed. (John Wiley and Sons, New York, 1975).
[62] Cauchy's formula (http://scienceworld.wolfram.com/physics/CauchysFormula.html) gives n^{air}, the index of refraction of air. With κ_m^{air} taken to be equal to 1, $\kappa_e^{\mathrm{air}}=\sqrt{n^{\mathrm{air}}}$.
[63] T. Soné, Philos. Mag. **39**, 305 (1920).
[64] Y.-C. Lai, C. Grebogi, R. Blümel, and M. Ding, Phys. Rev. A **45**, 8284 (1992).
[65] A. Kohler and R. Blümel, Phys. Lett. A **238**, 271 (1998).
[66] C. Clark, SIAM Rev. **9**, 627 (1967).
[67] A. Kohler and R. Blümel, Ann. Phys. (N.Y.) **267**, 249 (1998).
[68] *Handbook of Mathematical Functions*, edited by M. Abramowitz and I. A. Stegun (Dover, New York, 1972).
[69] B. Sauer, K. A. H. van Leeuwen, A. Mortazawi-M., and P. M. Koch, Rev. Sci. Instrum. **62**, 189 (1991).
[70] A. Kohler, Ph.D. thesis, Albert-Ludwigs-Universität Freiburg i. Br. (Fakultät für Physik) 1998 (unpublished).
[71] We did explore the use of large Teflon bars. However, we were aware from F. Rosebury, *Handbook of Electron Tube and Vacuum Techniques* (American Institute of Physics, New York, 1993), p. 513 (see also http://www.andersonmaterials.com/tma.htm), that Teflon PTFE (polytetrafluoroethylene) changes its volume by 1% or more at a temperature near 20 °C (i.e., near room temperature!) compared to Teflon FEP (fluorinated ethylene-propylene). We could not risk such a change occurring in the cavity after the Teflon was (supposedly) machined to "final" dimensions. Stocking distributors we queried were unsure whether their Teflon plate stock was PTFE or FEP and were even unaware of the issue. Coupled with the expense of a relatively large quantity of Teflon, this discouraged us from further consideration of Teflon for the present experiment.
[72] Though we did not directly measure κ_m^w, the relative magnetic permeability of the wax, we did place wax samples next to a Rb optical pumping cell and found no detectable shift (<1 part in 10^4) of the 205 kHz magnetic resonance of ^{85}Rb in the magnetic field of the room. We expect κ_m^w to be close to the vacuum value $\kappa_m \equiv 1$ and unaffected by nuclear-magnetic-resonance effects that, for protons in the earth's field, occur at kilohertz frequencies [E. M. Purcell, H. C. Torrey, and R. V. Pound, Phys. Rev. **69**, 37 (1946)], far below the gigahertz frequencies of our RS measurements.
[73] A. F. Harvey, *Microwave Engineering* (Academic Press, London, 1963).
[74] It is important to amplify the signal from the receiving antenna. Trying, instead, to amplify the power sent into the transmitting antenna gave spurious results. The cause is harmonics generated in the incident-power amplifier. Whenever the fundamental frequency *or one of its harmonics* passes through a resonance frequency of the cavity, the receiving antenna produces a signal, and it is incorrect to associate this only with the fundamental frequency. Absent further information, one does not know if the signal comes from the fundamental or from a harmonic. Measurements with a spectrum analyzer showed that harmonics generated by our synthesizer alone are sufficiently far down in power to avoid such problems.
[75] A. Richter, Phys. Scr., T **90**, 212 (2001).
[76] *Landolt-Börnstein: Physikalisch-Chemische Tabellen*, edited by R. Börnstein and W. Roth (Springer, Berlin, 1912), pp. 341, 343.
[77] M. J. Davis and E. J. Heller, J. Chem. Phys. **75**, 246 (1981).
[78] W. A. Lin and L. E. Ballentine, Phys. Rev. Lett. **65**, 2927 (1990).
[79] S. Tomsovic and D. Ullmo, Phys. Rev. E **50**, 145 (1994).
[80] S. D. Frischat and E. Doron, Phys. Rev. E **57**, 1421 (1998).
[81] C. Dembowski, H.-D. Gräf, A. Heine, R. Hofferbert, H. Rehfeld, and A. Richter, Phys. Rev. Lett. **84**, 867 (2000).
[82] D. A. Steck, W. A. Oskay, and M. G. Raizen, Science **293**, 274 (2001).
[83] W. K. Hensinger, H. Häffner, A. Browaeys, N. R. Heckenberg, K. Helmerson, C. McKenzie, G. J. Milburn, W. D. Phillips, S. L. Rolston, and H. Rubinsztein-Dunlop, Nature (London) **412**, 52 (2001).
[84] R. Hofferbert, H. Alt, C. Dembowski, H.-D. Gräf, H. L. Harney, A. Heine, H. Rehfeld, and A. Richter, Phys. Rev. E **71**, 046201 (2005).
[85] S. Sridhar, Phys. Rev. Lett. **67**, 785 (1991).
[86] C. E. Porter, *Statistical Theories of Spectra: Fluctuations* (Academic Press, New York, 1965).
[87] M. L. Mehta, *Random Matrices and the Statistical Theory of Energy Levels* (Academic Press, New York, 1967).
[88] M. L. Mehta, *Random Matrices*, 2nd ed. (Academic Press, New York, 1990).
[89] T. Guhr, A. Müller-Groeling, and H. A. Weidenmüller, Phys. Rep. **299**, 190 (1998).
[90] M. V. Berry, Proc. R. Soc. London, Ser. A **400**, 229 (1985).
[91] G. Casati, B. V. Chirikov, and I. Guarneri, Phys. Rev. Lett. **54**, 1350 (1985); M. Feingold, *ibid.* **55**, 2626 (1985).
[92] Feingold (Ref. [91]).

[93] G. P. Berman and G. M. Zaslavsky, Phys. Lett. **61A**, 295 (1977).
[94] M. Roederer, A. Treister, W. Moore, and L. A. Herzenberg, Cytometry **45**, 37 (2001).
[95] H. Poincaré, *Les Methodes Novelles de la Mechanique Celeste* (Gauthier-Villars, Paris, 1892).
[96] D. Zagier, Math. Intell. **0**, 7 (1977).
[97] http:/www.msri.org/publications/In/msri/1998/mandm/ sarnak/1/ is a video recording of a lecture by P. Sarnak that includes discussion of the widespread importance of counting prime numbers.
[98] D. Rockmore, *Stalking the Riemann Hypothesis: The Quest to Find the Hidden Law of Prime Numbers* (Pantheon, New York, 2005).
[99] R. Schäfer, U. Kuhl, M. Barth, and H.-J. Stöckmann, Found. Phys. **31**, 475 (2001).
[100] M. V. Berry, in *Structural Stability in Physics*, edited by W. Güttinger and H. Eikemeier (Springer-Verlag, Berlin, 1979), pp. 51–53.
[101] M. L. Lapidus, Trans. Am. Math. Soc. **325**, 465 (1991).
[102] R. Devaney, *A First Course in Chaotic Dynamical Systems* (Addison-Wesley, Reading, MA, 1992).
[103] E. Ott, *Chaos in Dynamical Systems* (Cambridge University Press, Cambridge, U.K., 1993).
[104] V. G. Veselago, Usp. Fiz. Nauk **92**, 517 (1967) [Sov. Phys. Usp. **10**, 509 (1968)].
[105] D. R. Smith, J. B. Pendry, and M. C. K. Wiltshire, Science **305**, 788 (2004).
[106] Y. Décanini and A. Folacci, Phys. Rev. E **68**, 046204 (2003).